Joint Centre for Mesoscale Meteorology, Reading, UK

Interaction of mesoscale tropopause depressions with a warm-core cyclone: observational and model analysis and sensitivity to analysis errors

K. A. Browning
A. J. Thorpe
A. Montani
D. Parsons
M. Griffiths
P. Panagi
E. M. Dicks

Internal Report No. 101

February 1999

Met Office Joint Centre for Mesoscale Meteorology Department of Meteorology
University of Reading PO Box 243 Reading RG6 6BB United Kingdom
Tel: +44 (0)118 931 8425 Fax: +44 (0)118 931 8791
www.metoffice.com

Designed and produced by the Met Office © Crown copyright 2001 01/0240 The Met Office logo is a registered trademark.

Version dated 11 Feb 99

Interaction of mesoscale tropopause depressions with a warm-core cyclone: observational and model analyses, and sensitivity to analysis errors.

K.A. Browning[1], A.J. Thorpe, A. Montani, D. Parsons[2], M. Griffiths, P. Panagi, and E.M. Dicks

University of Reading

Abstract

This paper focuses on the coupling between the warm core of an ex-tropical cyclone and 2 pre-existing mesoscale tropopause depressions (TDs), ie downward intrusions of stratospheric air. The TDs approached the cyclone from widely separated sources after becoming cut off from different upper-level troughs upstream of it.

The first part of the study reported here combines Meteosat imagery with products from the limited-area version of the operational UK Met Office Unified Model to reveal the 3-dimensional structure and evolution of the mesoscale features. Each TD was a potential vorticity (PV) anomaly characterised by dry-intrusion air descending beneath an upper-level jet streak. Each TD generated its own cloud head and each is believed to have contributed to the deepening of the surface cyclone.

[1] Corresponding author: Joint Center for Mesoscale Meteorology, Department of Meteorology, University of Reading, RG6 6BB, UK. (The Joint Center for Mesoscale Meteorology is supported by the Meteorological Office and the Department of Meteorology, University of Reading. The research has been undertaken under the auspices of the UK Universities Weather Research Network funded by the Natural Environment Research Council).

[2] On leave from the National Center for Atmospheric Research, Boulder, Colorado, USA.

Later parts of the paper identify errors in model forecasts and attribute them to analysis errors in the position of one of the TDs. We have used two methods to locate the analysis errors. Both are capable of being used in real time. The first is the identification via satellite imagery of an error in the Met Office model's water vapor analysis, and its translation into thermal and kinematic information via PV inversion. The second method, using singular vectors calculated for the ECMWF model, involves the identification of sensitive regions where any analysis error would be expected to grow rapidly. In the case studied here the regions highlighted by these two methods were essentially co-located. The present case is unusual in that the most sensitive region was in the upper troposphere and apparently associated with a tropopause depression. Forecast reruns made with the Met Office and ECMWF models after modifying the upper-level PV in the analysis showed some limited improvements.

1. Introduction

There is a large body of literature describing the cyclogenesis that results from the coupling of upper tropospheric features with low-level baroclinic zones (see the review by Uccellini 1990). Accurate prediction of cyclone development depends on the ability of operational numerical weather prediction (NWP) models to represent such coupling processes in detail. A particular problem, especially over data-sparse ocean areas, is to ensure that the features are properly represented in the model analyses. Thus much thought is currently being given (1) to devising methods of using satellite imagery to identify and apply adjustments to the model analyses (Mansfield 1997, Carroll, 1997, Demirtas and Thorpe 1998) and (2) to establishing the feasibility of making extra observations targeted on the regions that are predicted to be sensitive to errors in the initial analysis (Snyder 1996, Joly et al 1997, Montani et al 1999). To underpin the development of such techniques it is desirable to obtain a better understanding of the 3-dimensional structure of the interacting components of the cyclone system

and to examine the relationship of these dynamical components to the predicted regions of sensitivity of forecasts to errors in the initial structure: these are the objectives of the paper.

The paper presents a diagnostic study of a developing cyclone and brings together three methodologies: satellite imagery interpretation as pursued by Weldon and Holmes (1991) and Bader et al (1997), 'potential vorticity (PV) thinking' and attribution applied to NWP model output as advocated by Hoskins et al (1985), Fehlmann and Davies (1997), Thorpe (1997), and Griffiths et al (1999), respectively, and singular-vector analysis as a means of identifying regions where the cyclone forecasts are particularly sensitive to errors in the initial state (Buizza and Montani 1998). We use output from operational runs of the nominally 60-km grid, limited-area version of the UK Met Office Unified Model (Cullen 1993) and the imagery from the infrared and water vapor channels of Meteosat. For the singular vector analyses the T69 version of the ECMWF model is used.

The event analysed in this paper is an Atlantic cyclone in October 1996 that originated as Tropical Cyclone Lili. The cyclone track and a surface analysis are shown in Fig.1. We study the cyclone just after its transition to an extra-tropical cyclone, which occurred at about 0 UTC, 27 Oct (27/0). The broad-scale evolution of the cyclone and its detailed mesoscale structure at the time of peak intensity have been analysed by Browning et al (1998). At peak intensity the cyclone produced severe gales and heavy rain over the British Isles and it still retained a warm core up to 400 hPa. Unified Model analyses and very-short-range (T+6) forecasts verified well against continuous wind profiler measurements in Wales during the time of peak intensity. Here we shall be more concerned with the earlier re-intensification period of the cyclone, between 27/12 and 28/06.For this period, when the cyclone was over the data-sparse ocean and the model performance was poorer (though still useful), we shall use Meteosat imagery as best we can to establish the model errors.

Mesoscale tropopause depressions corresponding to tropopause folds, hereafter referred to simply as tropopause depressions or TDs, played a key role in the re-intensification process. There were two dominant TDs. One (TD1) originated as a cut-off from a large-scale trough to the west of the cyclone: see the small shaded area at 26/06 centerd at 53°W and 41°N in Fig 2(a). Twenty-four hours later TD1 had moved eastward and was situated just behind the cyclone at 36°W and 46°N (Fig.2(b)). Subsequently another tropopause depression, TD2, became cut-off from the large-scale trough to the north of the cyclone and it then followed behind TD1 as they both interacted with the cyclone. This paper is about these interactions.

In Section 2 we introduce a conceptual model of the organization of the ascending and descending circulations within a mature cyclone as it couples with a single tropopause depression. In Section 3, the full complexity of the dual TD interactions are examined in the real case. Key features of the structure of the intensifying cyclone as seen in the satellite imagery and in the model analyses are described first. Then we focus on the individual TDs and their evolution before and during their interaction with the cyclone. The model analyses reproduced the broad features quite well and are used without adjustment to describe the structure and evolution of the TDs in Section 3. However, errors in the model analyses were large enough to affect significantly the accuracy of the forecasts.

In Section 4 we describe the forecast errors for the 24-h forecast that embraced the period of cyclone reintensification. This is done for the Unified Model forecast. We then look at the corresponding ECMWF forecast run and use the known forecast errors (ie known after the event) to estimate the analysis errors applicable at the start of that particular forecast run. This is done by projecting the known errors in the ECMWF forecast onto the dominant singular vectors and then using the so-called pseudo-inverse method (Montani 1998). We also show the results of an ECMWF forecast rerun with these errors removed to confirm that the diagnosed analysis error

is indeed sensible.

We then address the question, in Section 5, as to whether we could have estimated the analysis error using only information available at analysis time. First we use WV imagery to estimate analysis errors in the upper-level PV field. Then we look at the singular vector analysis to identify the region to which the forecast was most sensitive to analysis errors. The location of this so-called sensitive region is shown to coincide with the main region of analysis error identified from the imagery.

Finally, in Section 6, we use the PV modification technique in the form described by Griffiths et al (1999) to apply the adjustment determined from the WV imagery to see if the resulting reanalysis gives rise to an improved forecast. This leads us to conclude that there is some potential in the PV-WV approach, at least in those cases where the analysis error is predominantly at upper levels. In some future operational scenarios it may be possible to supplement this approach with data from targeted unmanned aircraft directed to regions identified either from the singular vectors or the WV imagery.

2. A conceptual model of the cyclone structure during coupling with a single tropopause depression

To set the scene, Fig. 3 shows some general features of the structure of a cyclone during coupling with a *single* tropopause depression. This figure is based on the idealized model in Fig. 1 of Browning et al (1995) but it has been adapted in order to relate better to the case analysed in the present paper. (The main difference is that in the previous model the flows were more elongated in the front-parallel direction owing to the stronger stretching deformation in that case. Also the orientation of the pattern has been rotated cyclonically to correspond to the rather non-standard orientation of the pattern in the present case). The model in Fig. 3 consists of two interlocking flows: a dry-intrusion flow (Browning 1997) and a moist high-θ_w flow (θ_w is wet-bulb

potential temperature). To a first approximation these flows are mirror images of each other in the vertical, but laterally displaced. The ascent of the high-θ_w flow is responsible for the upper parts of a cloud head (Böttger et al 1975, Browning and Roberts 1994a), whose top rises towards a characteristically curved convex outer boundary CC. The mainly descending dry-intrusion flow originates from the region of the tropopause depression. As shown in the cross-section XX', the stratospheric part of the dry intrusion descends as a tropopause fold into the middle and lower troposphere. Air of upper tropospheric origin near the tropopause fold also descends and gives rise to an extension of the dry intrusion which reaches down to the boundary layer close to the associated cold front. This conforms to the model of Danielsen (1964) (reproduced in Fig.1. of Browning 1997). Whereas the frontal structure in the vicinity of WW' corresponds to that of an ana-front, that near XX' corresponds to a kata-front characterised by less high cloud and often not much precipitation.

The structure of the case in the present paper will be shown to conform to the model in Fig.3 but it is more complicated in that there were two sets of partially overlapping structures of this kind. Actually there were more than two but our analyses will concentrate on the two major ones associated with the two tropopause depressions, TD1 and TD2. In Section 3 we show that each of these was associated with its own PV streamer (S1 and S2), dry intrusion (D1 and D2), cold front (CF1 and CF2), upper-level jet (J1 and J2) and cloud head (CH1 and CH2). This duality obviously complicates the interpretation but is something that has to be taken into account in practical forecasting situations because it occurs often. Double structure of this kind was, for example a feature of the FRONTS-92 cyclone analysed by Browning et al (1995 and 1997) but the duality in the present case was more pronounced and more easily resolved. In cases such as this the question arises as to which, if any, tropopause depression is going to interact with a cyclone and with what consequences. We go on to address this question in Sections 4 and 5.

3. Analysis of the structure of the cyclone during its re-intensification phase

(a) The cloud heads as seen in the satellite infra-red imagery

The Meteosat infrared images in Figs. 4 (a), (b) and (c) show, near the center of the frame, the cloud tops associated with the cyclone at 27/12, 28/0 and 28/12, respectively. These times span the main period of re-intensification during which there were two major cloud heads. The cloud heads rotated cyclonically with time, the orientation shown in the idealized model in Fig. 3 corresponding to that near the beginning of the period.

At the initial time (27/12), shown in Fig. 4(a), the cloud head is the western-most, relatively smoothly-curved, extension of the band of cloud (grey in this image) trailing westward from the British Isles (ignoring the patch of bright, high cloud north of 55°N between 10 and 20°W). The cloud head extends from 47 to approximately 52°N and from 20 to 27°W, with its convex outer boundary (cf.CC in Fig.3) facing west. The cyclone center is at the southeastern tip of the cloud head (at 22°W, 47.5°N). The top of the cloud can be seen sloping upwards (ie darkening) from east to west in the eastern half of the cloud head. By analogy with the airflow analysis of a cloud head in Browning and Roberts (1994a), we may expect this to be associated with westward-directed system-relative slantwise ascent within it (as in Fig. 3). The cloud head in Fig.4(a) is the first of the two main cloud heads and is refered to as CH1.

At the end of the period of re-intensification (28/12), shown in Fig. 4(c), a new cloud head (CH2) extends from 6.5 to 23°W and from 54 to 50°N, with its convex outer boundary (CC) facing south. The cyclone center is over Ireland, close to the northward-directed hook of cloud at the eastern end of the cloud head. High-θ_w air now enters this cloud head, rising slantwise from north to south, and again fanning out towards the reorientated boundary CC.

In the hooked part of the cloud head over Ireland this air-flow curves cyclonically first towards the east and then north. As shown by Browning et al (1998) the hook was a region of heavy rain with severe gales on its flank.

Between the two times depicted in Figs. 4(a) and (c) there was a period when both cloud heads were detectable simultaneously as, for example, at 28/0 in Fig. 4(b). The original cloud head, CH1, is associated with the higher (brighter) streaks of cloud at this time, with its convex outer boundary CC extending from 14°W, 52°N to 26°W, 55°N. The new cloud head, CH2, is developing at a lower level just to the south of CH1, its tops rising smoothly from a region of very shallow (dark grey) layer-cloud between 15 and 19°W along the 50° latitude up to mid-tropospheric levels close to the edge of CH1 at 23°W, 53°N. The outlines of the southern (CC) boundaries of these two cloud heads are drawn in Fig.4(d), along with other information discussed shortly. (Other cloud features in Fig.4(b) extending from CH2 as far west and south as 30°W and 50°N, respectively, are convective shower clouds and a more organized finger of cloud orientated northeast-southwest which, like CH2, are associated with TD2.) Water-vapor imagery corresponding to the time of Fig. 4(b), shown later in Fig.5(b), depicts CH2 as a weak (ie not very bright) feature probably because at this time it was not only shallow but also overlain by very dry stratospheric air associated with parts of the tropopause depressions, TD1 and TD2.

The infrared image in Fig.4(d), is for the same time as the infrared image in Fig.4(b) but it has a different grey scale to enhance the contrast within the narrow temperature range +12 to +2°C. This enhancement draws attention to two boundaries, First, it shows the clearance of cloud following the passage of the first cold front (CF1) associated with CH1. Secondly, it shows the arrival of shallow boundary-layer cumulus clusters associated with the advection of increasingly cold air arriving behind the second cold front (CF2) that was associated with CH2. This interpretation is consistent with surface analyses, and also with NWP model results discussed in Section 3(c).

Also shown in Fig.4(d) are the axes of the upper-level parts of dry intrusions D1 and D2 as inferred from the Meteosat water-vapor imagery. The evidence from the WV imagery is shown shortly, in Section 3(b). Then, in Section 3(c), we show NWP model evidence that connects these dry intrusions with the corresponding surface cold fronts, as in the model in Fig.3: essentially the dry upper-level air was descending down isentropic surfaces inclined at roughly 1 in 100.

(b) The dry intrusions and associated upper-level jet streaks as inferred from the satellite water vapor imagery

The Meteosat water vapor images for 27/1830 and 28/0030 in Figs. 5(a) and (b), respectively, show dark zones surrounding the cloud head west of Ireland. Such dark zones show the location of dry air in the upper and middle troposphere (Weldon and Holmes 1991). The axes of these dark zones, identified by dotted lines, are associated with dry intrusions labelled DO, D1 and D2. Examination of a sequence of images like those in Fig. 5 (not shown) reveals how these dry intrusions are advected cyclonically around the cyclone center. The dark zones D1 and D2 are due to the two main dry intrusions which we later show to be related to tropopause depressions TD1 and TD2, and to cloud heads CH1 and CH2. In Section 5(a) , we compare the positions of these dark zones with corresponding dry features in the model: this provides confidence in the model's ability to represent such features at all, whilst at the same time quantifying errors in the precise position of one of these features in the model.

Between each of the dark zones (dry intrusions) identified in Figs. 5(a) and (b), there are lighter grey wedges of moist air, possibly with small remnants of dissipating cirrus in some of them. These correspond to the warm moist wedges of Weldon and Holmes (1991). They draw attention to the well known fact that the edges of the moist wedges in these circumstances correspond to jet streaks. The same relationship applies in the

present case as shown by the model-derived 300-hPa windspeeds depicted in Fig.6. The jet streaks JO, J1 and J2 in Fig.6 are seen to be located just in advance of the corresponding dry-intrusion axes, D0, D1 and D2 in Fig.5(a). Although the dark zones show up in the imagery as relatively narrow axes of dry air aloft, we shall show in Sec.3(c) that the associated dry intrusions were extensive layered features that undercut the moist air in the jet streaks (the moist wedges) as they descended towards the boundary layer.

An interesting complication revealed by Fig. 6 is that J2 was in two parts at 27/18. As we shall show in Section 3(e), TD2 was just beginning to interact with the cyclone's warm core at this time, and the leading edge of its PV anomaly was starting to deviate eastwards toward the cyclone. As this occurred, part of the associated jet streak, which previously had been entirely on the right (western) flank of the southward-moving TD2, transferred to the southern edge of the eastward-moving leading part of TD2. This is consistent with the formation of the small west-east orientated part of J2 shown in Fig 6. Six hours earlier there had been no sign of this part of J2, and even at the time of Fig. 6 it is still not well defined. However, six (twelve) hours later, this part of J2 elongated and increased in speed to over 35 (45) m s^{-1}, whilst the speed of the original, trailing part of J2 had decreased to 30 (25) m s^{-1}. The reason for the break in J2 is related to the distortion of the shape of the PV anomaly associated with TD2 as it interacted with the cyclone. The gap between the two parts of J2 corresponded to a region of very strong cyclonic curvature so that in this region the high value of PV was accompanied by strong curvature instead of strong shear and an associated jet.

(c) The 3-dimensional structure of the dry intrusions

The positions of dry intrusions aloft as deduced from the WV imagery and of surface cold fronts as deduced from IR imagery are plotted together in Fig. 4(d). It was suggested in Sec. 3(a) that the dry-intrusion air-flows descended slantwise from the WV dark zones forwards to the surface cold

fronts consistent with the idealized model in Fig. 3. The detailed evidence for this is given in the model-derived cross-section shown in Fig. 7 which is orientated along AA' in Figs. 4(d) and 5(b).

The dominant feature in Fig. 7 is the long (dark grey) finger of dry air associated with dry intrusion D2 which brings air with relative humidity less than 10% down to 700 hPa. Figure 7 shows that D2 is associated with a PV streamer (centered on the 300K isentrope) with values of 1PV unit also coming down to 700 hPa. (Notice that the axis of the PV streamer lags slightly behind that of the dry intrusion; this should be taken into account when using the WV imagery to validate the model's PV structure. The tendency for such a mismatch to occur has been pointed out by Mansfield (1997).) Similar fingers of dry-intrusion air are evident in parallel sections (not shown) on either side of that in Fig. 7, showing that they are part of a broad curtain of descending air that fans out behind the surface position of the cold front in the hammer-head pattern discussed by Danielsen (1964) and Young et al (1987), and sketched here in Fig.3.

Dry intrusion D2 was behind dry intrusion D1, and also D0, and it was undercutting both of them at the time of Fig. 7. The sections farther north depict D1 and D0 more clearly, but they can nevertheless still be seen in Fig. 7 as (dark grey) dry fingers extending below 500 hPa at ranges between 1300 and 2000 km. However, the upper parts of D1 and D2 are partly obscured by moist air overrunning them near 300 hPa, associated with jet streaks J1 and J2 as labelled in Fig. 7. These moist patches centered at 300 hPa correspond to the 'moist wedges' referred to earlier in connection with the WV imagery in Fig.5(a).

(d) Potential vorticity associated with the dry intrusions

The PV anomaly (PV1) associated with D1 was well marked in successive model analyses when viewed in suitable sections, and that

associated with D2 even more so. Values of PV in excess of 1PV unit were shown in Figs. 7 to have descended as low as 700 hPa in association with D2 but the PV anomaly associated with D1 is less clear in this particular section. In fact the PV anomalies are most easily identified in plan sections, at the higher levels. In order to follow the evolution of PV features we find it best to portray the PV in a constant-pressure surface, especially that at 300 hPa. For some purposes it is preferable to view PV within constant -θ surfaces where it is more nearly conserved. In the present study we prefer to view PV features within constant-pressure surfaces (or height of PV = 2 units, Mansfield 1997) precisely because temporal changes in the PV anomalies reflect changes in the intensity of the tropopause depressions. We shall analyse these temporal changes in the next section but first we show a snapshot of the 300-hPa pattern of PV at 27/18 (Fig.8), at a time that corresponds to the satellite WV image in Fig.5(a).

Figure 8 shows that the model resolved three 300-hPa PV maxima associated with TDs encircling the cyclone: TDs 0, 1 and 2, respectively, display closed contours of 3.5, 5 and 7 PV units. Each PV maximum was a dry feature distinct from the column of diabatically generated PV situated at lower levels within the cyclone. And each PV maximum is seen in Fig. 8 to be located at the end (closest to the cyclone) of PV streamers, labelled S0, S1 and S2 which radiate outwards from the cyclone center and correspond to features seen in the WV imagery. Specifically these streamers are associated with corresponding dry intrusions (D0, D1, D2) and jet streaks (J0, J1, J2) depicted in Figs. 5 and 6, respectively. Plan sections at lower levels (not shown) demonstrate that the PV streamers are sections through curtains (layers) of maximum PV that slope downwards towards the south and east in the same manner as the dry intrusions.

As we shall show in Section 3(e), the 300 hPa PV cores retained a clear identity when tracked over a long period (more than a day). We shall henceforth concentrate on analysing the PV cores corresponding to TDs 1

and 2 rather than their associated streamers S1 and S2. These TDs are situated around the convex outer boundary (southwestern boundary) of the cloud heads and associated warm core. We show in Section 3(e) that TD1 and TD2 were associated with the development of cloud heads CH1 and CH2. But first we analyse the relationship of the two TDs to the cyclone center.

(e) Evolution of the mesoscale tropopause depressions and their interaction with the cyclone.

The relationship between the TDs and the cyclone is shown in Fig. 9. The figure is in 5 parts. The first part (a) shows the tracks of the 300-hPa PV cores corresponding to TD1 and TD2, and of the cyclone center, relative to the Earth; the parts (b) and (c), respectively, show the tracks of TD1 and TD2 relative to the cyclone center at 27/18, with the model's cloud head and coastlines shown for the corresponding time. The two TDs could be tracked unambiguously through successive 6-hourly model analyses. As noted earlier in connection with Fig.2 they came from different large-scale troughs: TD1 from the western trough and TD2 from the northern trough. In each case the track of the TD in the model began to deviate once the center of the TD came within 700 km of the cyclone center, at which stage the leading edge of its PV anomaly would have been approximately above the outer boundary of the cyclone's warm core. Thereafter each TD adopted a track which took it cyclonically around the southern boundary of the warm core.

Figure 9 (b) shows that TD1 began to deviate at 27/06 (Time code 5). It then skirted around the cyclone until 28/18 (Time code 11). Figure 9(d) shows that the peak value of PV at 300 hPa was between 2.5 and 3.5 PV units until 27/12. It then increased to (and thereafter remained) between 5 and 5.5 PV units presumably as a result of descent accompanying interaction with the cyclone's warm core.

Figure 9 (c) shows that tropopause depression TD2 began to deviate at 27/18 (Time code 7). (The apparent growth in the area of TD2 at this time is illusory : as explained in the figure legend, different PV contours are used at different times and a lower-valued PV contour was used at this time).This deviation happened as TD2 became elongated, with a new PV core developing at 300 hPa, 300 km ahead of the original TD2 core (see dumbell shape of PV at time 7). Figure 9(c) shows that the new core associated with TD2 was an off-shoot from the original TD2 core and its development at the expense of the original core appears to have been due to differential vertical motion in its vicinity. The newly descending PV core at this time was associated with the development of the new (leading) part of jet streak J2 as discussed earlier in Section 3(c). The relationship between the elongation of PV centers in troughs and PV gradients, jet streaks and upper-level fronts is discussed in Davies and Rossa (1998) and references therein. Figure 9 (c) shows that the new part of TD2 encircled the cyclone from 27/18 until (and beyond) 28/18 (Time code 7). Figure 9(d) shows that TD2 was characterised by a large 300-hPa PV of 6 units from the very beginning. It then fluctuated between 6 and 8.5 units, before stabilizing at close to 7.5 units as it skirted the cyclone, i.e. it did not strengthen significantly while interacting with the cyclone's warm core.

The two TDs, once their motion had begun to deviate upon coming close to the cyclone, followed rather similar tracks around its warm core. Thus the position of TD2 at 28/0 was almost identical to that of TD1 12 hours earlier. By 28/12 the position of TD2 was similar to that of TD1 6 hours earlier. This does not imply that TD2 was catching up with TD1 because by this time their velocity was increasing such that TD2 remained about 300 km behind TD1.

The behaviour of the two main mesoscale tropopause depressions may be summarised as follows:

(i) The two TDs were cut off from two separate troughs upwind of the cyclone.

(ii) Both began to deviate perceptably in their motion when they came close to the edge of the cyclone's warm core. We hypothesise that this deviation is an indication that the TDs were beginning to couple with the warm core.

(iii) After coupling they followed similar tracks relative to the cyclone, encircling the southern flank of its warm core : TD2 followed about 300 km behind TD1.

(iv) TD1 had a peak value of about 3 PV units at 300 hPa before coupling but this increased to about 5 units following coupling, implying substantial descent. TD2 retained a value of about 7 units throughout.

(v) The increase in the 300-hPa PV of TD1 which took place between 27/12 and 27/18 (Figure 9(d) occurred at the same time that the msl pressure of the cyclone began to decrease (Figure 9(e).

A diagramatic summary is given in Table 1 to clarify the timing of the above events and their relationship to the occurrence of the two cloud heads discussed in Section 3(a). Although there is some subjectivity in identifying the precise duration of the cloud heads, the evidence in Table 1 strongly suggests a link between the coupling of TD1 with the cyclone and the development of cloud head CH1, and similarly between TD2 and CH2. In other words CH1 developed just after TD1 started to deviate toward the cyclone and, similarly, CH2 developed just after TD2 started to deviate toward the cyclone. The period of cyclone deepening appears to overlap the two coupling events. There may have been two separate cyclone centers during the period when two cloud heads coexisted but neither the model nor the sparse observations over the ocean was able to resolve them.

It is probably significant that the cyclone underwent a large and abrupt

Table 1: Summary of cyclone evolution during interaction with the two mesoscale tropopause depressions

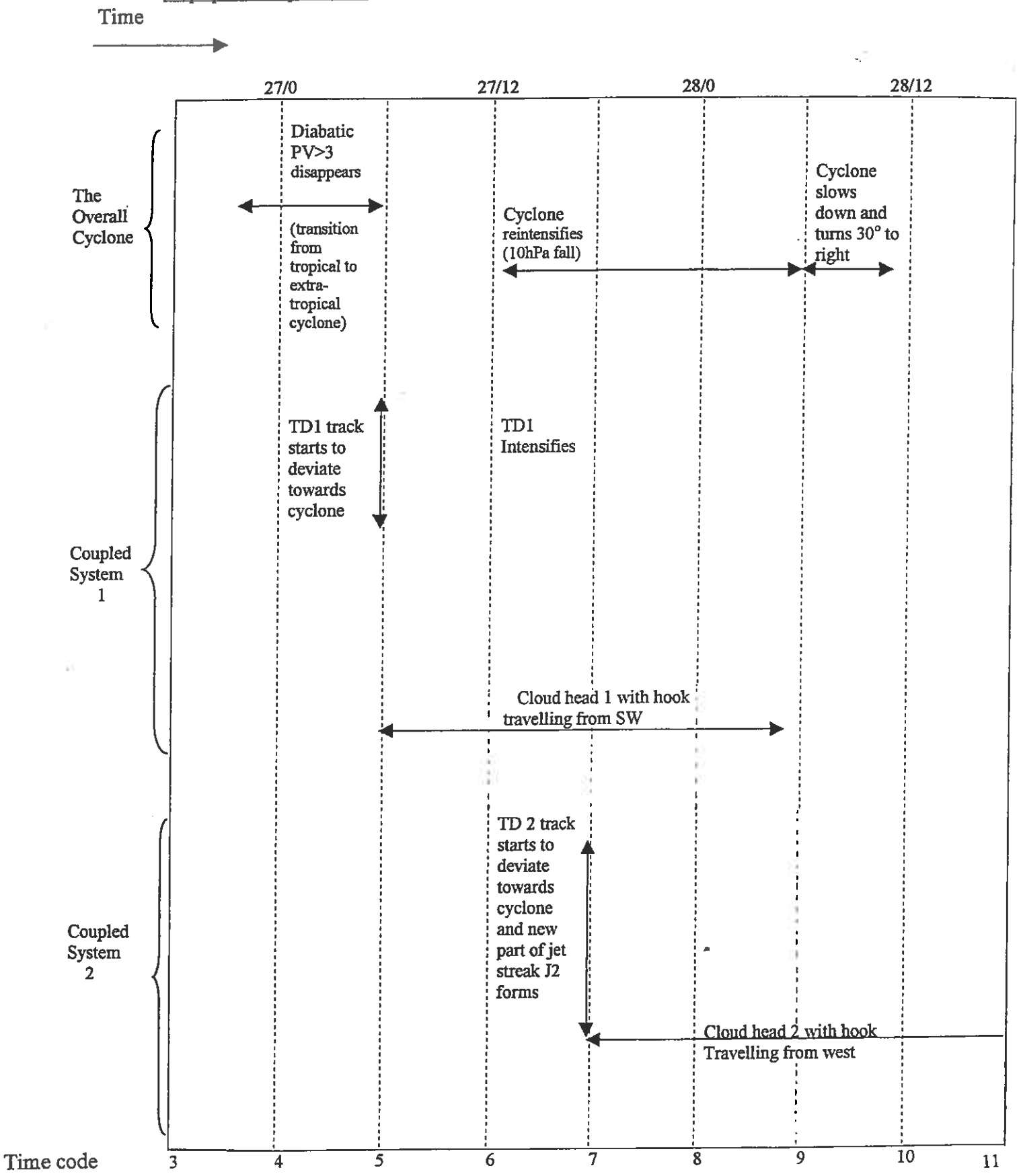

change in velocity (it almost halved its speed and turned more than 30 deg to the right) after CH1 gave way to CH2. We speculate that the discontinuity in velocity was due to TD2 superceding TD1 as the dominant upper-level influence.

We further speculate that there may have been some direct or indirect coupling between TD1 and TD2. There are two steps in the argument. First we suggest that the coupling of TD1 with the cyclone was responsible for the initial reintensification of the cyclone. This is supported by the fact that TD1 intensified at the same time that the cyclone itself began intensifying (see Table 1). As a result we suggest, secondly, that the intensified cyclone would then have interacted more strongly with TD2 when it subsequently came within range. This is supported by the fact that the track of TD2 began to deviate toward the cyclone when the cyclone was already 6 hours into its intensification phase. The authors visualise the interactions metaphorically as follows : TD1 behaves as a picador in triggering the cyclone (the Bull) into some initial development; then the stronger matador (TD2) comes along and finishes the job i.e. causing the main period of development, not killing it (although the cold dry air which TD2 brought with it may have subsequently hastened its demise).

4. Errors in NWP model forecasts of the cyclone and the implied analysis errors

(a) The errors in the 27/12 forecast run of the operational model

We shall now examine the forecast for the critical period of intensification and attempt to identify and account for its deficiencies. We limit our consideration to the forecast period out to T+24 and to the run commencing at 27/12. At earlier times the forecasts were occasionally bad because they involved interactions between the cyclone and spurious upper-level features (Carroll 1997). Within the time range we have chosen, the

forecasts were at least suggesting interactions with the appropriate tropopause depressions. In such circumstances it is possible to make some useful deductions about the factors leading to the error growth.

Figure 10 shows the location and msl pressure of the cyclone center between 27/12 and 28/12, as derived from successive 12-hour analyses (crosses connected by solid lines) and the corresponding forecasts from the 27/12 forecast run (circles connected by dashed lines). Evidently the forecast position of the low center was 150 km in error by 28/0 and this error doubled in the next 12 hours. More significantly, although the forecast did identify some deepening from 27/12 to 28/0, the rate of deepening was too slow by a factor of 4.

A hypothesis to account for the underdevelopment of the cyclone in the 27/12 forecast run is that it is due to the upper-level PV anomaly associated with TD2 being mispositioned. The mispositioning is evident from a comparison between the T+12 forecast (Fig.11(a)) and the corresponding analysis for 28/0 (Fig.11(b)). The leading part of TD1, with a 300hPa PV of 4.5 PV units, is close to 20°W, 51°N in both analysis and forecast. The main difference is in the position of TD2 which in the forecast is centered 250 km farther away from the cyclone(x). Subsequently in this forecast TD2 was left behind as the cyclone continued travelling to the northeast, and no interaction took place.

The actual cyclone slowed down greatly and turned to the right between 28/06 and 28/12 and this was attributed in Section 3(e) to the influence of TD2. The failure of the forecast cyclone (Fig.10) to change its velocity or to deepen significantly is believed to be due to the forecast position of TD2 being too far away from the cyclone to have any influence.

(b) Use of known forecast errors to infer the analysis errors.

Up to this point all of the model data used in this paper have been from the Unified Model LAM. However, we shall now use results from a study using the T-69 version of the ECMWF model, in which singular vector (SV) analysis has been applied to cyclone Lili (see Montani (1998) for further details). The analysis from the ECMWF model differed greatly from those from the LAM before 27/12 (possibly because of different treatment of a bad observation at 26/12) but for the initial period of cyclone development from 27/12 to 28/00 the two models agreed more closely in their analyses: the central pressure of the surface low agreed to within 2hPa albeit with a positional error still as large as 200 km at 27/12. We shall now use results obtained from the 27/12 ECMWF forecast run to infer the analysis errors at 27/12 that would account for the observed (ie known after the event) forecast errors at 28/12.

We use localized singular-vector computations as described in Buizza and Montani (1998). With this method it is possible to find the location of the region, typically 24, 36 or 48 hours before the valid time of a forecast, where any analysis error would have grown rapidly to reduce the skill of the forecast over a selected target zone. This region is referred to as the 'sensitive region'. To make this computation in the case of cyclone Lili, a target zone was defined (10°W to 5°E and 45°N to 60°N) containing the cyclone at 28/12 (the "final time"). The SVs were then computed for a number of different "initial times" but we restrict the discussion here to those computed 24 hours earlier, at 27/12.

We shall discuss later, in Section 5(b), the horizontal and vertical structure of the first singular vector as a way of identifying the sensitive region in real time. In the present section we shall instead invoke the pseudo-inverse technique (Buizza et al 1997) as a means of estimating the analysis errors knowing the forecast error. First, the ten most rapidly growing SVs were calculated from the forecast from 27/12 verifying at 28/12. These SVs maximize the growth of total energy over this time period over the region of

the cyclone at 28/12. The forecast error was then projected on the SVs and these projections were used at analysis time to estimate the analysis errors. This allowed us to calculate the PV adjustment needed at analysis time to improve the forecast. The resulting PV adjustment field at 400 hPa is represented in Fig.12 by the thin contours the maximum of which can be seen to be centered 600 km south of the 400 hPa PV maximum corresponding to TD2 (and 700 km west of the much weaker TD1). The sign of the adjustment is such as to imply a slight (up to 0.5 PV units) enhancement on the southern flank of TD2 in the modified rerun. In terms of adjustments to the geopotential height, a 1.6 dam intensification of the 500 hPa trough is implied in the same region.

Confirmation of the improvement in the 24-hour forecast achieved using the above adjustment is given in Fig. 13. This shows that the error in the forecast mean-sea-level pressure of the cyclone center decreases from 7 hPa in the operational run (Fig. 13a) to 2 hPa in the modified rerun (Fig. 13b) when compared with the ECMWF analysis in Fig. 13(c) (which was itself 4 hPa greater than the corresponding LAM analysis). In addition, the analysed location and shape of the storm, eg the strong pressure gradient south and west of the cyclone (Fig. 13c), are represented better in the modified run (Fig. 13b) compared with the operational run (Fig. 13a).

In view of the improvement in the 24-hour forecast of msl pressure achieved by applying the adjustment in Fig. 12, it is worthwhile also considering the associated changes in positions and intensities of the upper-level PV maxima. Figure 14 shows the 300 hPa PV distribution at 28/12 from (a) the operational 27/12 forecast run and (b) the 27/12 forecast run made using the modified analysis. Comparison with the analyses in (c) shows that the modified forecast brings the PV maximum somewhat farther east and 200km closer to the cyclone center (which is itself brought farther west). However, the modified forecast still greatly underestimates the forward advance and intensification of the PV maximum shown in Fig. 14(c).

The pseudo- inverse method provides only an approximate estimate of analysis error. This is partly because only a limited number of SVs are used. Also the growth of the SVs is linear and dry, whereas growth of perturbations in the full forecast model is, of course, non-linear with full model physics. Therefore it is not surprising that the forecast reruns are still not perfect. With the first 10 singular vectors we expect to explain at most 29% of the forecast error and so this is probably an upper bound on how much of the analysis error we can find. In fact we find that, in the 24-hour ECMWF forecast verifying at 28/12, the rms error in the 1000 hPa geopotential height field decreases from 20.0 m in the operational run to 16.5 m in the perturbed run. The corresponding decrease in rms error at 500 hPa was from 27.2 m to 16.0 m. This translates to an overall improvement of 18% at 1000 hPa and, surprisingly, as much as 41% at 500 hPa. This suggests that the pseudo-inverse technique has indeed found part of the actual analysis error.

5. The possibility of assessing analysis errors from information available at analysis time only.

(a) Identification of errors in the model analyses using water vapor imagery

Information from satellite WV imagery relating to the pattern of upper tropospheric humidity was not used in the operational NWP model analyses and can therefore be used as an independent check on the analyses. In order to evaluate the model analyses against the satellite imagery we have generated a sequence of pseudo-WV images from successive model analyses. Codes exist which calculate in detail the WV-channel radiance that would be expected from the model-derived distribution of moisture and cloud (eg Schmetz and van de Berg 1994). For the purpose of this study, however, we have adopted the simple expedient of deriving pseudo-WV imagery by averaging the model's relative humidity at 300, 400, 500 and 600 hPa and comparing the resulting patterns with the real imagery as in Browning and

Roberts (1994b). One of the resulting images is reproduced in Fig.15.

The pseudo-WV image in Fig 15 corresponds (within 30 mins) to the actual WV image in Fig.5(a). The differences between these two images are partly attributable to the choice of grey scales. However, the most obvious discrepancy is in the extent of the moist (white) area far to the north of the cyclone center (shown as a cross) and we suspect that the model's underestimate of its extent is largely due to the inability of our simple pseudo-WV algorithm to represent the effect of a shallow layer of cirrus cloud at the 300-hPa level. The model also fails to represent the hook of moisture just to the north-east of the cyclone center. The position of the main cloud head feature is about right, however. Also, the dark zones associated with dry intrusions DO, D1 and D2 are evident in both Figs. 15 and 5(a), where the axes of the dark zones are highlighted by lines passing through the darkest (driest) parts of the images. For the purpose of making detailed intercomparisons at various times, instead of reproducing more pseudo-WV images, we show in Fig.16 a sequence of tracings of the axis of one of the dry intrusions (D2) derived from the satellite (left (a)) and model analyses (right (b)). Also shown in (a) and (b), respectively, are outlines of the moist/cloudhead(s) derived from the WV imagery (shaded for brightness temperature less than 237 K) and from the model (shaded for mean relative humidity from 300 to 600 hPa more than 62.5%).

Agreement between the WV imagery and pseudo-WV imagery in Fig.16 is qualitatively quite good. Both show the dry intrusion D2 and an associated moist feature M2 (diagonally hatched in Fig.16) progressing cyclonically around the western and then southern flank of the main cloud head (diagonally hatched but with different orientation for the hatching). D2 and M2 themselves are situated on opposite sides of the maximum in PV (dotted area labelled V2 in Fig.16b)) associated with tropopause depression TD2. As noted above, the shape of the model's main cloud head differs in detail from that in the satellite imagery but its position is in reasonable

agreement, being on average perhaps 150 km too far south. The error in the model's dry intrusion D2 is more variable : it is 200 km too far north at the early times, but the error then diminishes to near zero at the later times in Fig 16. Similar agreement was found for dry intrusion D1 (not shown), although D1 was less well defined and the assessment more difficult to make. The broad overall agreement, in particular the fact that key features in the imagery are recognizable in the model, gives us confidence in the detailed model diagnoses in Section 3. However, the positional discrepancies are not negligible, especially at the earlier times. We now tie down these errors a little more precisely by comparing not only the dry part (D2) (as advocated by Mansfield 1997) but also the moist part (M2) of the vortex (V2) associated with TD2. In referring to the vortex V2 we are using shorthand for the high-PV anomaly in TD2.

The moist feature M2 in Fig 16, which we shall refer to as a moist head (by analogy with a similar feature analysed by Browning and Roberts 1994b), was part of the same vortex V2 that was also responsible for D2. Features M2 and D2 reflect the ascending and descending parts, respectively, of the circulation associated with V2. The interface between them corresponds to the axis of maximum PV, a cross-sectional view of which was shown earlier in Fig. 7. As can be seen from Fig.16(b), M2 and D2 rotate as a couplet around V2 as V2 itself skirts around the main cloud head. Comparison of Figs.16(a) and (b) shows that the model's error in locating M2 displays a similar trend with time to that for dry intrusion D2, albeit with slightly larger errors. We shall take the error in the midpoint of the combined M2/D2 couplet as the best available guide to the model's error in locating the vortex V2. This leads to the result that the model's error in the distance between V2 and the cloud head associated with the main cyclone is 300-400 km towards the north at 27/12 and 27/18. Since the model's cloud head may itself be a little too far north, for the purpose of the analysis that follows later we shall assume an error of 300 km at these times. This error decreases in later analyses to less than 150 km which is close to the error in the assessment.

The adjustment to the analysis suggested by the WV-PV technique is summarized in Fig. 17. The arrow in this figure shows the required 300 km displacement of TD2 superimposed on the operational (unmodified) 27/12 analysis. The apparent inconsistency between the north-south error identified here and the west-east error in TD2 identified in Fig. 11 can be reconciled by referring to Fig. 9. The analysed track of TD2 in Fig. 9(a) shows that TD2 was travelling southwards at 27/12 (Time code 6); it then interacted with the cyclone and by 28/00 (Time code 8) it was travelling in a more nearly easterly direction around the southern flank of the cyclone. The initial error corresponded to TD2 lagging behind its true position (ie it was too far away from the cyclone). The tendency to lag continued but the initial northerly error in TD2 tended to become more of a westerly error, with TD2 still too far away from the cyclone.

(b) Use of singular vectors to point to the sensitive region.

We have already presented, in Section 4 (b), the results of pseudo-inverse calculations based upon the singular vector analysis. This was done in order to estimate the analysis error given a knowledge of the error in the forecast. We now present the basic results of the singular vector calculations which would be available at, or prior to, the analysis time. Such results should be particularly valuable in determining the location of the sensitive regions. These are the regions where the forecasts could be expected to benefit from additional targeted observations. The vertical profile of total energy for the first SV (Fig.18) shows that the most sensitive region at 27/12 was at approximately 400 to 500 hPa, i.e. close to the level of the depressed tropopause. The high sensitivity found at this level helps to justify our preoccupation with the role of tropopause disturbances which is the underlying theme of this paper. It is, however, in contrast to the results of sensitivity studies for most other cases which tend to show greatest sensitivity in the lower troposphere (eg Montani 1998).

Figure 19 shows the horizontal structure of the first singular vector (ie the fastest growing singular vector) at 27/12 at 325 hPa and 400 hPa, superimposed on the basic state of PV. The structure of the SV exhibits a series of positive and negative perturbations, like a wave-train, elongated in the 'south-west to north-east' direction. Figure 12, obtained with the benefit of hindsight, suggested that the maximum analysis error at this time was at 48°N, 32°W. From Fig. 19 we see that this is within the region indicated by the first singular vector and is just to the south of the position of TD2 adjusted as indicated by the arrow in Fig. 17. In other words, the WV-PV and SV methods, although by no means in perfect agreement, do point to the same broad area in which the analysis required to be adjusted. Bearing in mind that this agreement is based upon two independent operational models (the ECMWF model and the Unified Model) this is quite encouraging.

In the next section we apply an adjustment to the initial PV field to see if it improves the forecast evolution. We do this using the Unified Model and for consistency we apply the 300 km displacement determined for that model in Section 5(a).

6. Effect of PV modification on the forecast.

The general hypothesis that a model forecast can be improved by modifying the PV field in accordance with errors in the initialization follows from the work of Mansfield (1997), Carroll (1997) and Demirtas and Thorpe (1998). We employ the PV inversion method described in Griffiths et al (1999) which is similar to that used by Demirtas and Thorpe (1998) and Fehlmann and Davis (1997). First we change the PV field over a limited area and then we use PV inversion to obtain new estimates of the wind and temperature fields from the modified PV field. The assumption for the inversion is the non-linear balance described in Davis and Emanuel (1991), with a lower boundary condition of the theta field being unaltered by the PV modifications. A difference between our work and that of Demirtas and

Thorpe (1998) is that we did not employ data assimilation and treat these modifications as bogus observations; rather we directly modified the analysis. This new analysis was used to initialize the Limited Area Model for a 24-hour forecast starting at 27/12.

The PV has been modified in the Unified Model analysis at 27/12 by displacing TD2 approximately 300 km towards the south between 500 and 250 hPa. The basis for a displacement of this magnitude was presented in Section 5(a). The PV modification actually applied, to correspond to such a displacement, is shown in Fig. 20 together with the operational PV field at 300 hPa. Although the overall sense of the modifications applied, both in the Unified Model (Fig. 20) and previously in the ECMWF model (Fig. 12), is such as to increase the magnitude of the PV to the south of TD2, an examination of the detailed modifications in these two figures shows that the changes are quantitatively quite different, with the largest increase in the PV field on Fig. 20 occurring more to the southeast of the centre of TD2.

The PV fields at 300 hPa calculated for the 24-h forecasts without (FOP) and with (FMOD) the southward displacement of TD2 are shown in Figures 21(a) and (b), respectively. The corresponding analysis is shown in Fig.21(c), at which time TD2 had an intensity of over 7.5 PV units and was located southwest of the Irish coast with high PV values associated with TD1 to the east of the low center at the surface. In FMOD (Fig. 21(b)) there is a deterioration in the location and magnitude of TD1 but a clear improvement in the depiction of TD2: the position of TD2 in FMOD is seen to be much closer to its analysed position (Fig. 21(c)) than it is in FOP (Fig. 21(a)), although its peak value of 6.5 PV units is somewhat too low. The displacement of TD2 closer to the cyclone suggests that it is in a better position to interact with it, although the lower value of its PV would tend to counteract this. These opposing influences may be part of the reason why the resulting improvement in the msl pressure field (not shown) was disappointingly small. The forecast of the central pressure for the modified forecast (FMOD) was essentially the

same as the forecast of 977 hPa for the unmodified operational forecast (FOP).

A practical computing problem we encountered may be part of the reason for the disappointing lack of improvement. Corruption of a data tape during the course of the research forced us to regenerate the operational analysis from the global fields but without access to the additional observational input. As a result, the so-called operational analysis shown by the thin contours in Fig. 20, whilst very similar to the genuine operational analysis shown in Fig. 17 (and producing a rather similar 24-hour forecast), does nevertheless exhibit some small differences. There is, in particular, a significant difference in the magnitude of the 300 hPa PV in the vicinity of TD1, which has a peak value of over 3.5 units in Fig. 17 compared with about 2.5 units in the regenerated operational analysis in Fig. 20. This might account for the deterioration in the representation of TD1 in the forecast run, FMOD, in Fig. 21(b), which in turn may have had a significant impact on the predicted cyclogenesis. There is, however, another possible reason for the lack of improvement in the modified forecast, which we explain next.

The method we have used to modify the analysis inserts only the non-divergent component of the wind in the modification region. It is thought that the associated divergent flow will develop in the initial stages of the forecast. If the forecast is over a relatively long period such as 48 or 60 hours, then this initial adjustment may not be important; however, this is less evidently so for a 24 hour forecast such as is carried out here. It is possible to validate the divergent wind from the PV inversion but this is not done here. Rather we have created an alternative control (FAC) wherein the unmodified PV is inverted and the forecast rerun, minus the divergent winds in the proposed modification region. The result of the FAC (not shown) was to degrade prediction of the low-pressure center from 977 to 979 hPa at 24-h. We draw two conclusions from this result. First, it is evident that the modification of the PV field has a greater positive impact than one would initially suspect from

comparison against the operational forecast (FOP) alone. In this context the relative deepening achieved by moving TD2 appears to have been about 2 hPa. The error in the FAC forecast with unmodified PV was about 9 hPa.

The more general implication of this result is that there is potentially a detrimental effect in the inversion process arising from ignoring the divergent component of the wind field. Simply recalculating the PV from the inverted quantities, as proposed by Fehlmann and Davies (1997), will not detect this type of shortcoming. The inclusion of the divergent component of the winds is possible within our formulation and this should be explored in future. Comparison between the operational forecast and the two simulations where PV inversion was used to derive the initial conditions show a pronounced reduction (which increased with time) in the low-level PV fields for the inverted simulations. Since this low-level PV feature was collocated with upward motions and the rainfall field, we suspect that this change is associated with the neglect of the divergent component.

Although we did obtain some deepening in the simulation with the modified PV (FMOD) relative to a proper control experiment (FAC), the magnitude of the improvement is still disappointing. To test whether this behaviour was due to errors in our estimation of the PV displacement, we conducted a series of separate sensitivity tests where the angle of displacement was varied from southerly to SSW and SSE and also where the displacement distance was halved (from 300 km to 150 km). The magnitude of the central low pressure varied by only about 1 hPa in these different experiments, suggesting that any modest errors in our estimation of the displacement of TD2 did not account for the lack of pronounced deepening in these forecasts.

7. Conclusions

Many strands of evidence have been brought together in this study,

both from observations (Meteosat) and from NWP models (the LAM version of the UK Met office Unified Model and the T-69 version of the ECMWF model). The findings and their interdependence may be summarized as follows:

(1) The reintensification of cyclone Lili shortly after becoming an extratropical cyclone was plausibly associated with its interaction with two mesoscale tropopause depressions, TD1 and TD2, that approached it after becoming cut-off from different troughs to the west and north of the cyclone, respectively.

(2) Each of these mesoscale tropopause depressions generated its own cloud head and each is believed to have contributed to the deepening of the surface cyclone

(3) Each mesoscale tropopause depression had a characteristic 3-D structure as seen in the Unified Model, with dry-intrusion air descending slantwise beneath its own upper-level jet streak.

(4) The mesoscale tropopause depressions could be identified from the patterns of upper-level moisture seen in the Meteosat water-vapor (WV) imagery. The second mesoscale tropopause depression, TD2, in particular, had a well-defined vortex-related WV signature which consisted of not only a 'dark zone' due to dry, upper-level air descending on the right hand side of the vortex, but also a corresponding 'grey zone', or 'moist head', due to moist air ascending on the left-hand side of the vortex. The WV signature has been used to identify errors in the model analyses of one of the mesoscale tropopause depressions.

(5) Both mesoscale tropopause depressions could be tracked at 300 hPa during a long series of model analyses as they approached and then coupled with the cyclone. The coupling was evident from a rather abrupt change in their

propagation velocity once they came within the radius of influence of the cyclone's warm core. After coupling, the two mesoscale tropopause depressions followed similar tracks around the right (southern) flank of the cyclone.

(6) The second and larger of the two mesoscale tropopause depressions, TD2, failed to couple in the 27/12 operational forecast run of the Unified Model. The 300 km error in the position of TD2 (identified as in (4)) was in the right sense (ie too far away from the cyclone) to account for its failure to couple.

(7) The deepening of the cyclone was significantly underestimated in the 27/12 forecast run and it is hypothesized that this was due to the estimated 300km error in the analysed position of mesoscale tropopause depression TD2. This hypothesis was tested by adjusting the position of the PV anomaly associated with TD2 using the technique of PV surgery. This achieved a perceptible improvement in the forecast track of TD2 . However the improvement in msl pressure was disappointingly small.

(8) The inference that the forecast error was due to a positional error of an upper-level feature in the analysis is supported by a singular vector analysis using the ECMWF model. The main sensitive region was identified just below 400 hPa and to the south of the main tropopause depression TD2. A corresponding analysis error implying a PV adjustment was identified using a pseudo-inverse technique, based on the known forecast error. When this estimated analysis error was removed a more realistic behaviour of the tropopause depression and a significantly improved forecast of the deepening of the cyclone occurred, thereby giving confidence in the identification of analysis errors.

The recent findings of Fehlmann and Davies (1997) and Demirtas and Thorpe (1998) indicate that distinct improvements in the model forecasts are possible when modifications are made to the PV field, particularly when the forecast errors are very large. The results of our PV surgery and singular vector analyses herein also suggest that modification of the upper-level PV fields can improve the model forecast. However, in this study, the impact on the deepening of the low center was small and the error in the position of the low was not greatly improved.

The relatively weak impact of modifying the PV distribution of the analysis is an important issue needing to be addressed further. Consideration of PV as a conserved quantity might lead one to suggest including very localised adjustments in the expectation that such adjustments would retain a spatial coherence. In fact there is a wave dispersion component which might tend to discourage one from making such localized modifications. Other factors that might explain the limited impact of modifying the PV distribution include (i) the possibly adverse effect of neglecting the divergent wind in the present PV inversion process, (ii) the impact of unmodified lateral boundary conditions for the Unified Model simulations and errors in the large-scale setting for the ECMWF model, iii) finite model resolution, as past work indicates that there is often a dependence of the prediction of the central low pressure on the horizontal grid spacing, iv) other errors in the three-dimensional depiction of the PV in the analysis, particularly in the lower and middle levels where PV is created by diabatic processes, and v) shortcomings in the model physics. In our case, the Unified Model and ECMWF model reruns both failed to improve the positioning of the low center. The formation of a second cloud head and deepening of the low near Ireland as the mesoscale tropopause depression TD2 approached suggest a type of secondary development that the models were unable to replicate. A valuable discussion of model errors for a case of secondary development off the coast of North America can be found in Gyakum et al. (1995).

Whilst acknowledging the need to reduce model errors, there is also a clear requirement, especially over data sparse areas such as the North Atlantic storm-track, to improve the analyses from which forecasts are made. We have used two methods in this study to locate analysis errors and to remove or at least reduce them. These methods can be used in real time. The first is the translation of an error identified (via satellite imagery) in the WV field into thermal and kinematic information via PV inversion. Using PV thinking allows both an identification of the existence of an analysis error as well as an estimation of that error. The second method, using SVs, is to calculate so-called sensitive regions where, if there is an analysis error, then this will grow rapidly. In order to reduce such an error, the use of pilotless aircraft to take additional localized observations would be an exciting possibility. In the case studied here the regions highlighted by these two methods were essentially co-located; it remains for further research to establish the generality of this result. In other cases of extratropical cyclones, such as observed in FASTEX, the sensitivity is probably more commonly in the lower troposphere rather than near tropopause level as in the present case, although even then there may be a clear dynamical link with nearby structures such as tropopause depressions.

References

Bader, M.J., G.S. Forbes, J.R. Grant, R.B.E. Lilley,. and A.J. Waters, 1995. *Images in weather forecasting,* Cambridge University Press, 499pp.

Böttger, H., M. Eckardt, and U. Katergiannakis, 1975 Forecasting extratropical storms with hurricane intensity using satellite information.

J.Appl.Meteor, **14** 1259-1265.

Browning, K.A., 1997 The dry intrusion perspective of extra-tropical cyclone development. *Meteor.Appl.,* **4**, 317-324.

Browning, K.A., and N.M. Roberts, 1994a Structure of a frontal cyclone *Quart.J.Roy.Meteor.Soc.,* **120**, 1535-1557.

Browning, K.A., and N.M. Roberts, 1994b Use of satellite imagery to diagnose events leading to frontal thunderstorms : part 1 of a case study. *Meteor.Appl.,* **1**, 303-310.

Browning, K.A., S.P. Ballard, and C.S.A.Davitt, 1997 High resolution analysis of frontal fracture. *Mon Wea.Rev.,* **125**, 1212-1230.

Browning, K.A., S.A. Clough, C.S.A. Davitt, N.M. Roberts, T.D.Hewson, and P.G.W. Healey, 1995 Observations of the mesoscale sub-structure of the cold air of a developing frontal cyclone,
Quart.J.Roy.Meteor.Soc., **121,** 1229-1254.

Browning, K.A, G. Vaughan, and P. Panagi. 1998: Analysis of an ex-tropical cyclone after its reintensification as a warm-core extratropical cyclone, *QuartJ.Roy.Meteor.Soc,* **124,** 2329-2356.

Buizza, R., R. Gelaro, F. Molteni and T.N. Palmer 1997 The impact of increased resolution on predictability studies with singular vectors. *Quart.J.Roy.Meteor.Soc.,* **123**, 1007-1033.

Buizza, R. and A.Montani, 1998 Targeting observations using singular vectors. *J.Atmos.Sci.,* **124,** Submitted.

Carroll, E.B. 1997 Poorly forecast trough disruption shown in water vapor images. *Meteor.Appl.*, ***4,*** 229-234.

Cullen, M.J.P. 1993 The unified forecast climate model, *Meteor.Mag.*, **122,** 81-94.

Danielsen, E.F. 1964 *Project Springfield Report,* Defence Atomic Support Agency, Washington D.C. 20301, DASA 1517 (NTIS # AD-607980), 97pp.

Davies, H.C., and A.M. Rossa, 1998 PV frontogenesis and upper-tropospheric fronts. *Mon.Wea.Rev.* **126,** 1528-1539

Davis, C.A. and K.A. Emanuel, 1991 Potential vorticity diagnostics of cyclogenesis, *Mon.Wea.Rev.*, **119**, 1929-1953.

Demirtas, M and A.J. Thorpe, 1998 Sensitivity of short-range weather forecasts to local potential vorticity modifications. *Mon.Wea.Rev.*, **124,** in press.

Fehlmann, R., and H.C. Davies, 1997 Misforecasts of synoptic systems: Diagnosis via PV retrodiction. *Mon.Wea.Rev.* **125.,** 2247-2264.

Griffiths, M., A.J. Thorpe, and K.A. Browning, 1999 Convective destabilisation by a tropopause fold diagnosed using potential vorticity inversion, *Quart.J.Roy.Meteor.Soc.*, **125**, Submitted.

Gyakum, J.R., and co-authors, 1995 First COMPARE Workshop: 5-9 October 1994. Montreal, Canada. *Bull.Amer.Meteor.Soc.*, **76**, 1209-1218.

Hoskins, B.J., M.E. McIntyre, and A.W. Robertson, 1985 On the use and significance of isentropic potential vorticity maps.

QuartJ.Roy.Meteor.Soc., **111**, 877-946.

Joly, A. and many others 1997 The Fronts and Atlantic Storm-Track Experiment (FASTEX) : Scientific objectives and experimental design *Bull.Amer.Meteor.Soc.,* **78**, 1917-1940.

Mansfield, D.A. 1997.The use of potential vorticity and water vapor imagery to validate numerical models. *Meteor.Appl.,* **4.,** 305-309.

Molteni, F., R.Buizza, T.N. Palmer and T. Petroliagis, 1996 The ECMWF ensemble prediction system : methololgy and validation, *Quart.J.Roy.Meteor.Soc.,* **122**, 73-119

Montani, A. 1998 Targeted observations for cases of cyclogenesis PhD thesis, University of Reading.

Montani, A ., A.J.Thorpe, R. Buizza and P. Under, 1999 Forecast skill of the ECMWF model using targeted observations during FASTEX. *Quart.J.Roy.Meteor. Soc.,* **125,** Submitted

Schmetz, J. and L. van de Berg, 1994 Upper tropospheric humidity observations from Meteosat compared with short-term forecast-fields. *Geophys.Res.Lett.,***21,** 573-576.

Snyder, C. 1996 Summary of an informal workshop on adaptive observations and FASTEX. *Bull.Amer.Meteor.Soc.,***77**, 953-961.

Thorpe, A.J., 1997 Attribution and its application to mesoscale structure associated with tropopause folds, *QuartJ.Roy.Meteor.Soc.,* **123**, 2377-2399

Uccellini, L.W. 1990. Processes contributing to the rapid development of

extratropical cyclones. In *Extratropical cyclones*, eds. C.W. Newton and E.O. Holopainen. Amer.Meteor.Soc., Boston, Mass.pp 81-105.

Weldon, R.B. and S.J.Holmes, 1991 Water vapor imagery, interpretation and applications to weather analysis and forecasting. *NOAA Tech.Report NESDIS 57,* 213pp.

Young, M.V., G.A. Monk, and K.A. Browning, 1987 Interpretation of satellite imagery of a rapidly deepening cyclone. *QuartJ.Roy.Meteor.Soc.,* **113**, 1089-1115.

Fig. 1

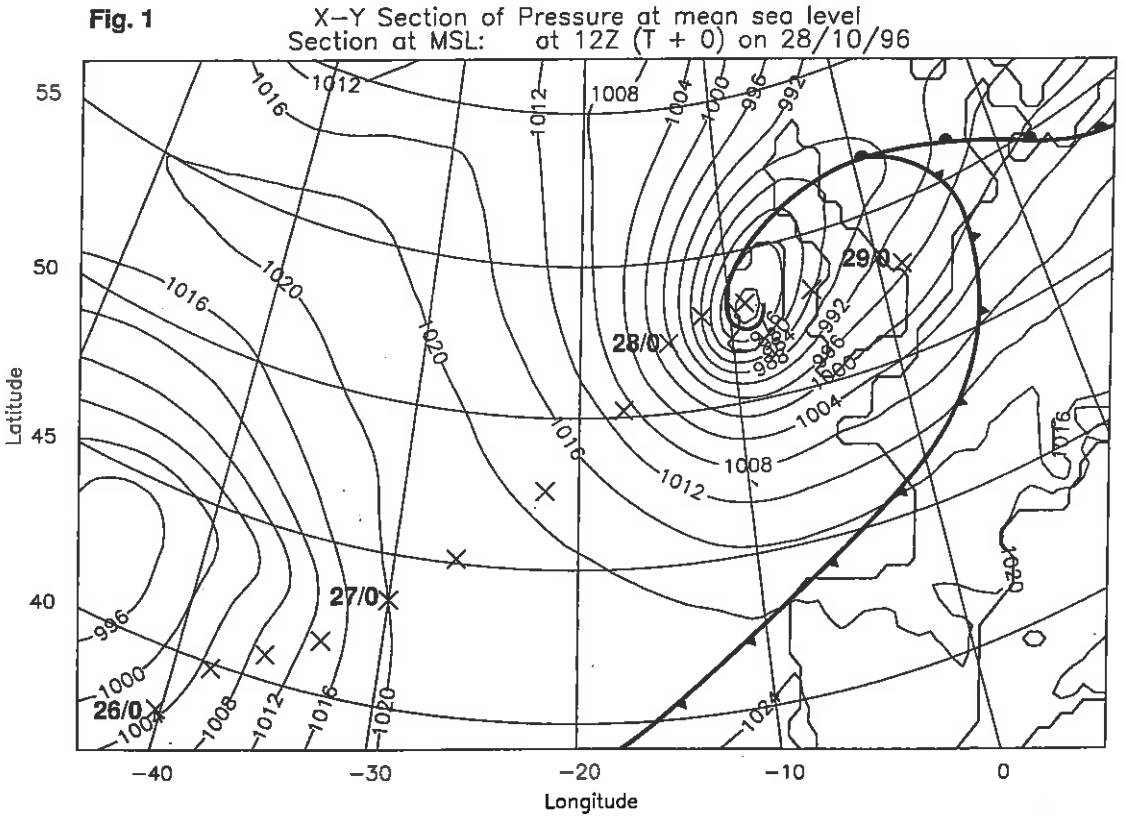

Fig.1 Mean-sea-level pressure from the UK Met Office Limited-Area model analysis and the corresponding operational Met Office frontal analysis for 12 UTC, 28 October 1996. Also shown are successive 6-hourly positions of the model's cyclone centre (crosses) from 0 UTC, 26 October until 0 UTC, 29 Oct.

Fig. 2 Tropopause height (in km), taken as the height of the 1.5 potential vorticity units surface, as derived from the UK Met Office Limited-Area model analyses for (a) 06 UTC, 26 October and (b) 06 UTC, 27 October 1996. Large shaded areas, with tropopause height less than 8km, draw attention to major upper-level troughs to the west and north of cyclone Lili, the msl pressure centre of which is denoted by X. The small shaded area, centred 15° west of the cyclone in (a) and 10° west of the cyclone in (b), is the mesoscale tropopause depression referred to as TD1 which has broken away from the western trough. Twelve hours after the analysis in (b) another mesoscale tropopause depression (TD2) broke away, this time from the northern trough, and it approached the cyclone behind TD1.

Fig 2(a)

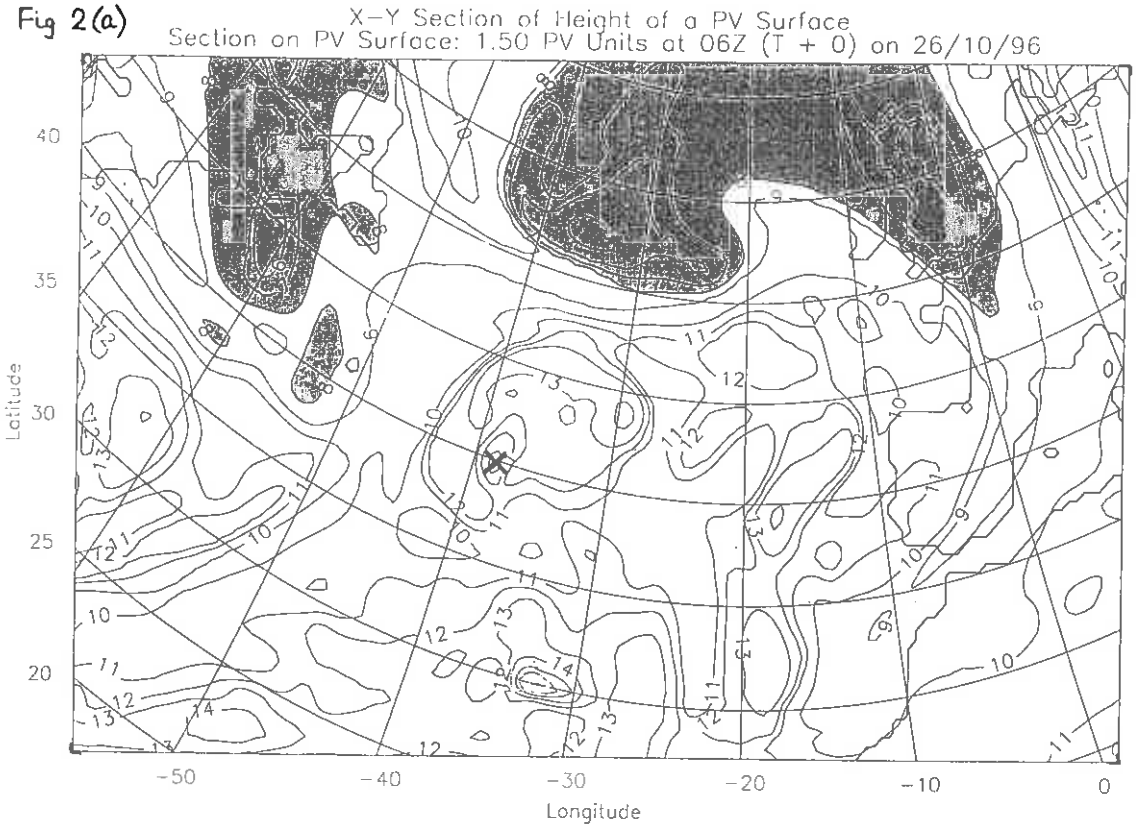
X–Y Section of Height of a PV Surface
Section on PV Surface: 1.50 PV Units at 06Z (T + 0) on 26/10/96
Latitude
40
35
30
25
20
−50
−40
−30
−20
−10
0
Longitude

Fig 2(b)

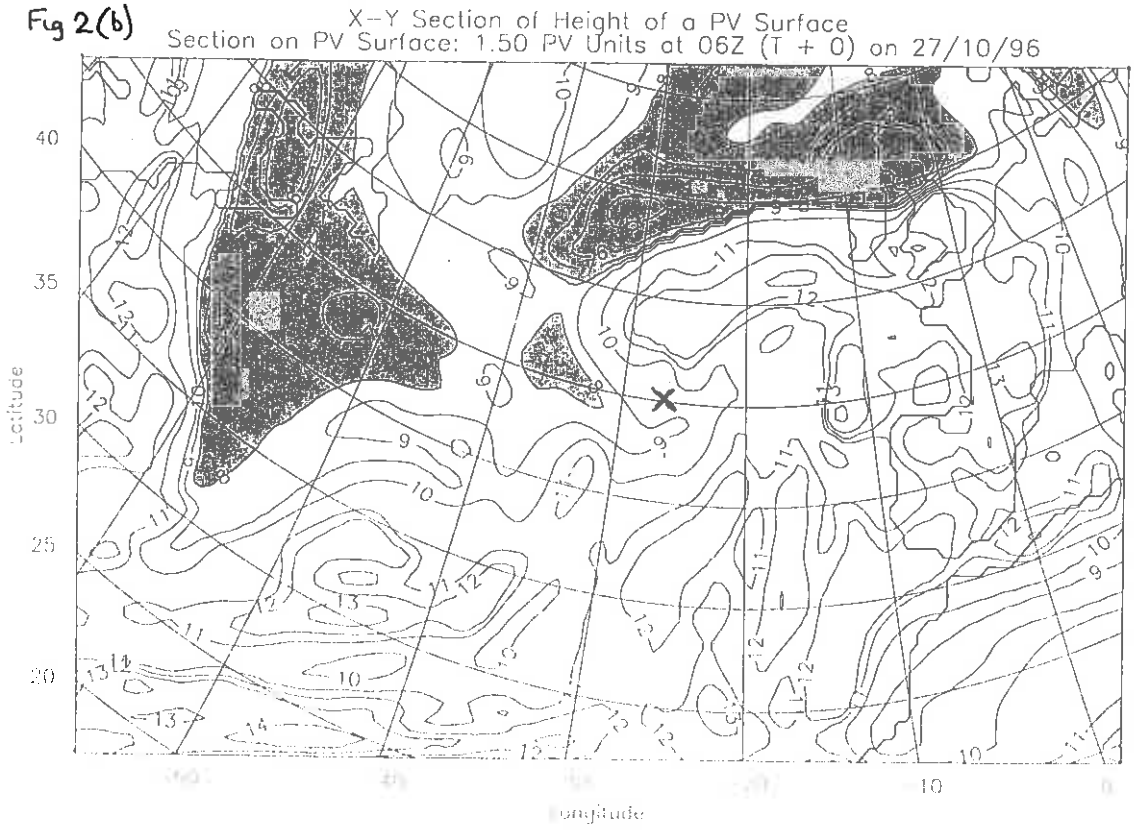
X–Y Section of Height of a PV Surface
Section on PV Surface: 1.50 PV Units at 06Z (T + 0) on 27/10/96
40
35
30
25
20
10
Longitude

Fig. 3

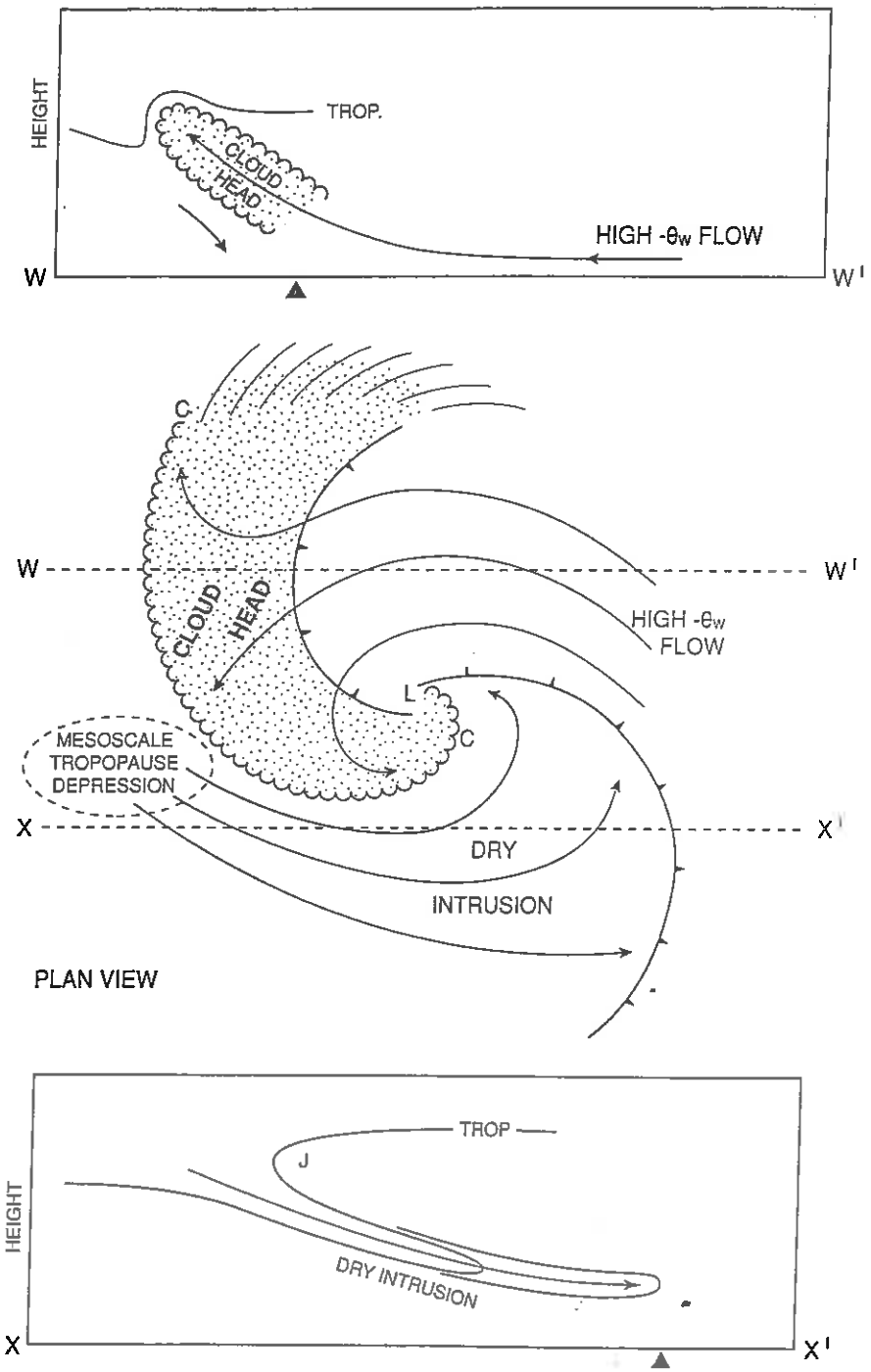

Fig.3 Idealized model showing the intertwining around a cyclone centre (L) of two rather symmetrical flows : the descending dry-intrusion flow (low wet-bulb potential temperature, θ_w and the ascending flow of high-θ_w air into the cloud-head (based on Fig.1 from Browning et al 1995). Middle part of figure is a plan view; upper and lower panels show vertical sections along WW' and XX', respectively. The black triangles in these sections denote the positions of the surface fronts.

Fig.4 Meteosat infrared images showing the cyclone at (a) 12 UTC, 27 October, (b) 0 UTC, 28 October and (c) 12 UTC, 28 October 1996. Brightness temperature scale (K) is shown on the right. The infrared image in (d) is for the same time as (b) but has a different grey-scale to emphasize the much narrower temperature range appropriate to the tops of boundary-layer clouds. Significant features in (a) and (c) are Cloud Head 1 (CH1) and Cloud Head 2 (CH2), whilst (b) shows both CH1 and CH2, as sketched in (d). Also drawn in (d) are the corresponding surface cold fronts, CF1 and CF2, and the upper parts of dry intrusions D1 and D2 as inferred from 'dark zones' in the water vapor imagery. AA' in (d) marks the end-points of the section in Fig.7.

Fig 4(a)

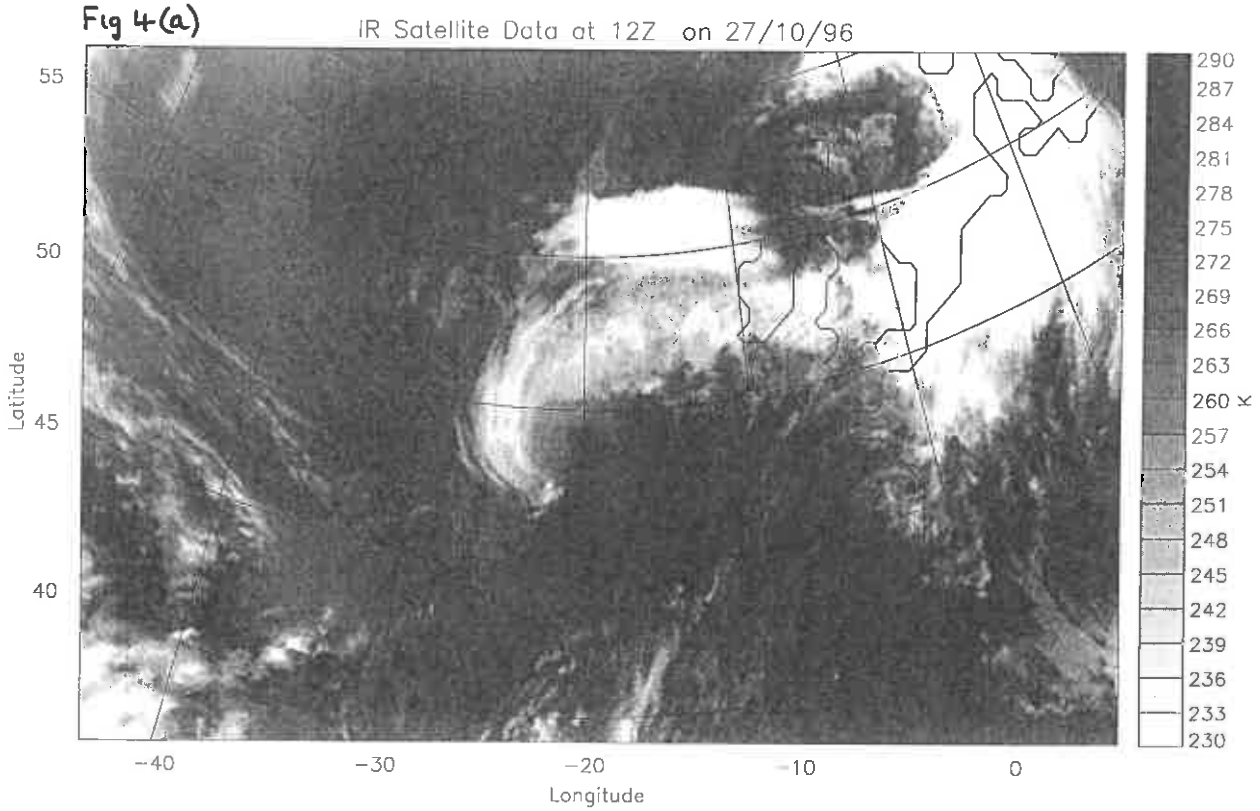
IR Satellite Data at 12Z on 27/10/96
55
50
45
40
Latitude
−40
−30
−20
−10
0
Longitude
290
287
284
281
278
275
272
269
266
263
260 K
257
254
251
248
245
242
239
236
233
230

Fig 4(b)

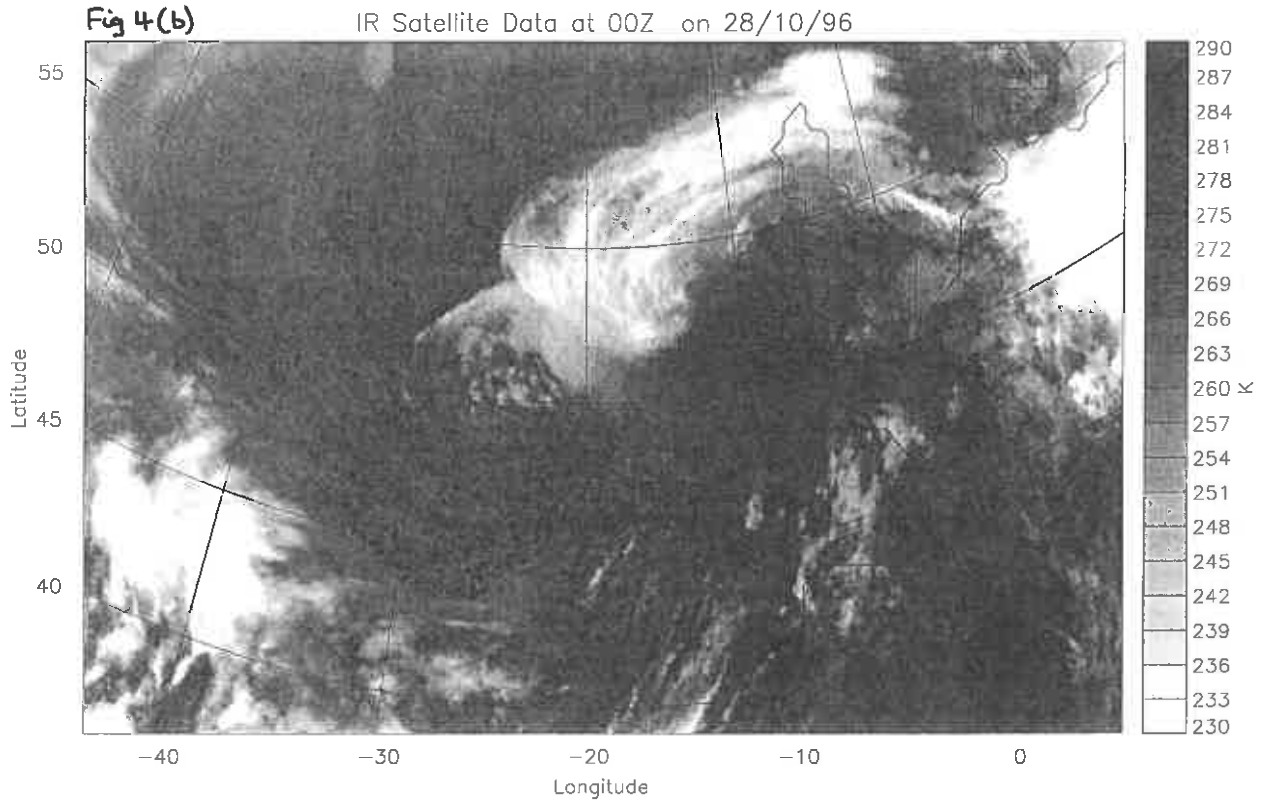
IR Satellite Data at 00Z on 28/10/96
55
50
45
40
Latitude
−40
−30
−20
−10
0
Longitude
290
287
284
281
278
275
272
269
266
263
260 K
257
254
251
248
245
242
239
236
233
230

Fig 4(c) IR Satellite Data at 12Z on 28/10/96

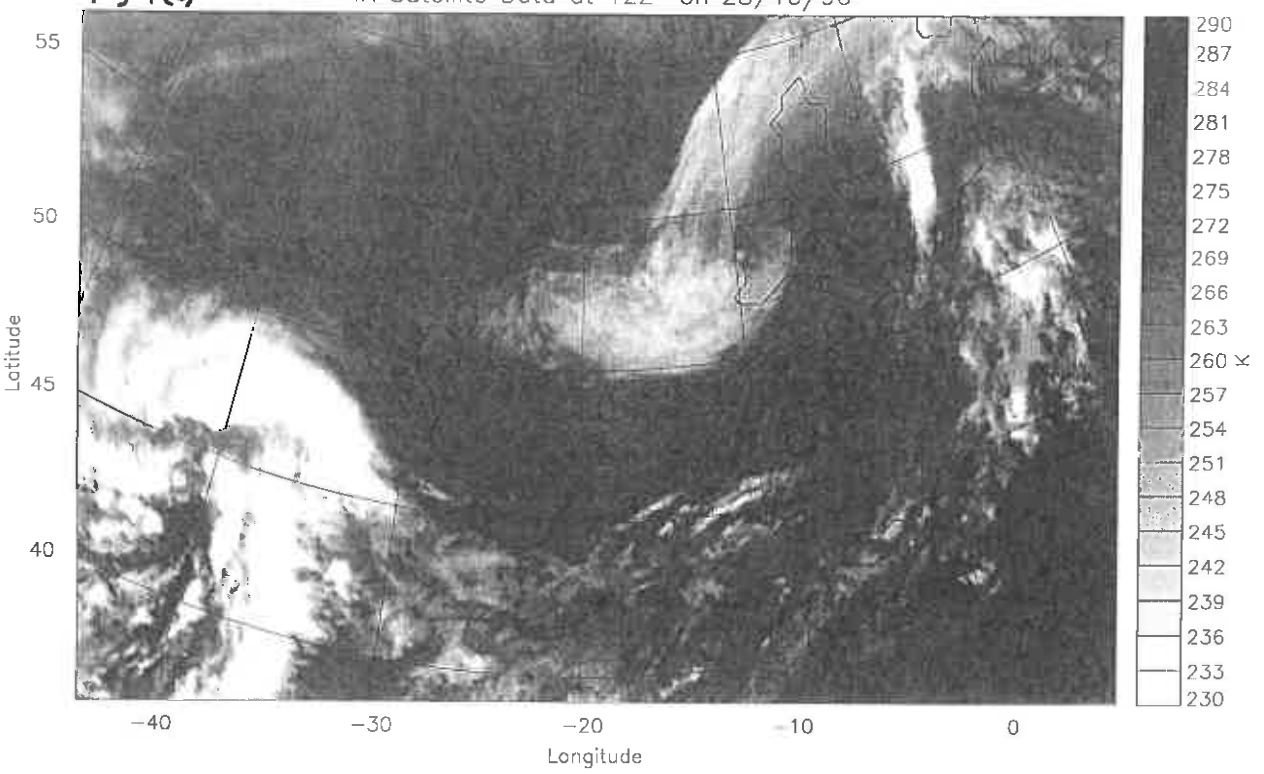

Fig 4(d) IR Satellite Data at 00Z on 28/10/96

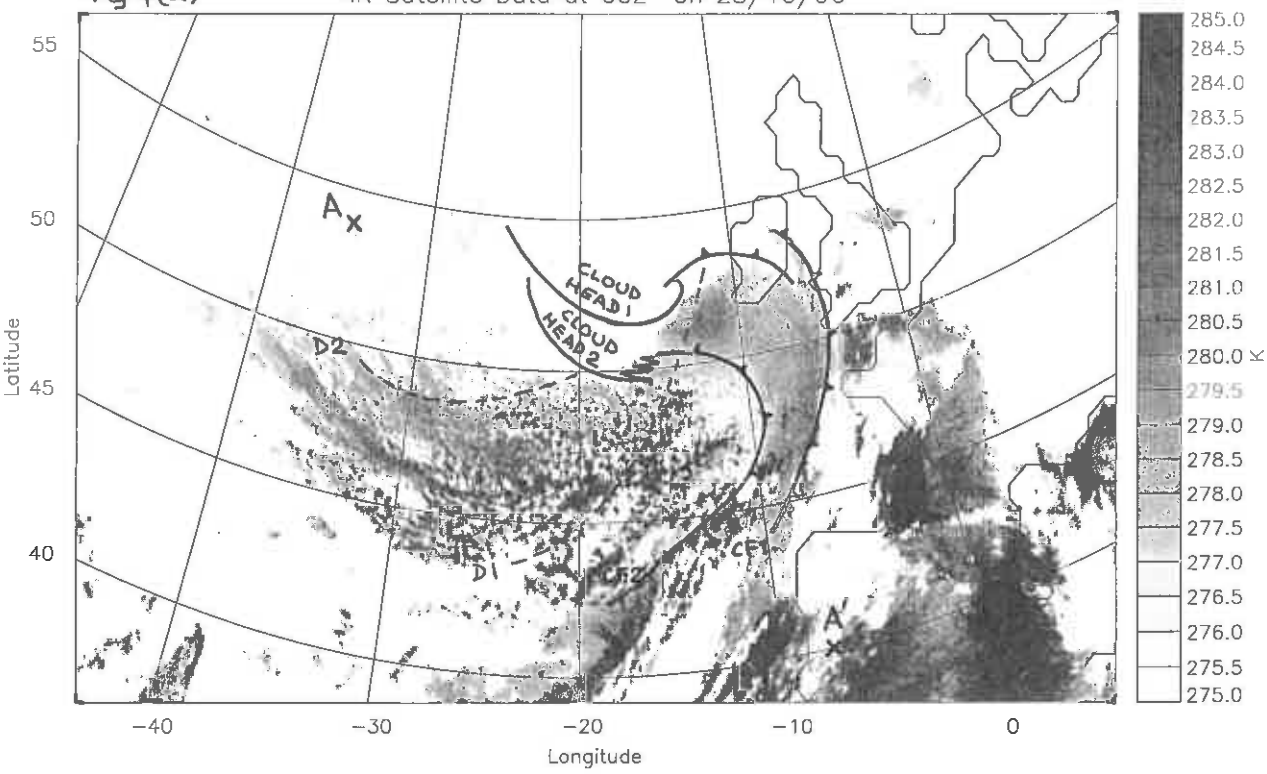

Fig.5 Meteosat water vapor images showing the distribution of upper-tropospheric water vapor (and cloud) associated with the cyclone at (a) 1830 UTC, 27 October and (b) 0030 UTC, 28 October 1996. The lone X marks the cyclone centre and the three dotted lines draw attention to the axes of three dark zones corresponding to the upper parts of dry intrusions DO, D1 and D2. AA' in (b) marks the end-points of the section in Fig.7.

Fig 5(a)

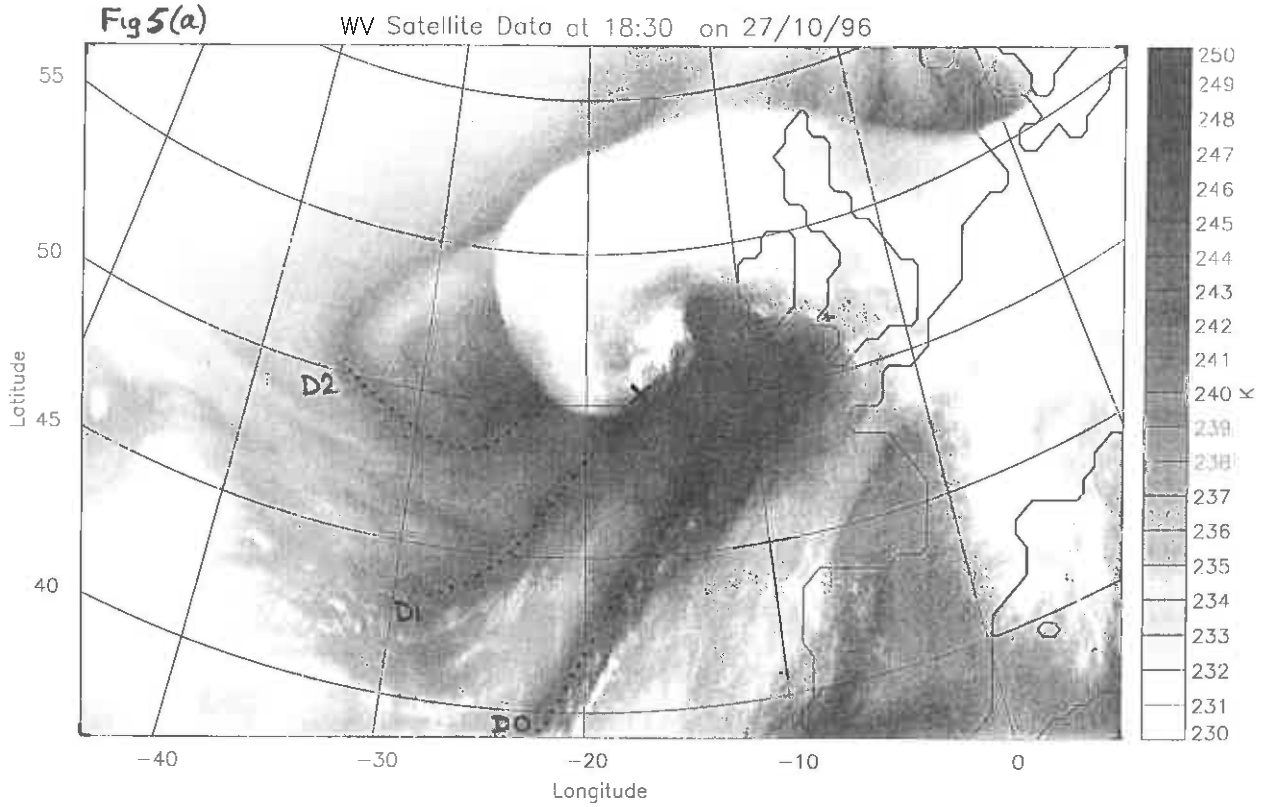
WV Satellite Data at 18:30 on 27/10/96
Latitude
55
50
45
40
D2
D1
D0
X
−40
−30
−20
−10
0
Longitude
250
249
248
247
246
245
244
243
242
241
240 K
239
238
237
236
235
234
233
232
231
230

Fig 5(b)

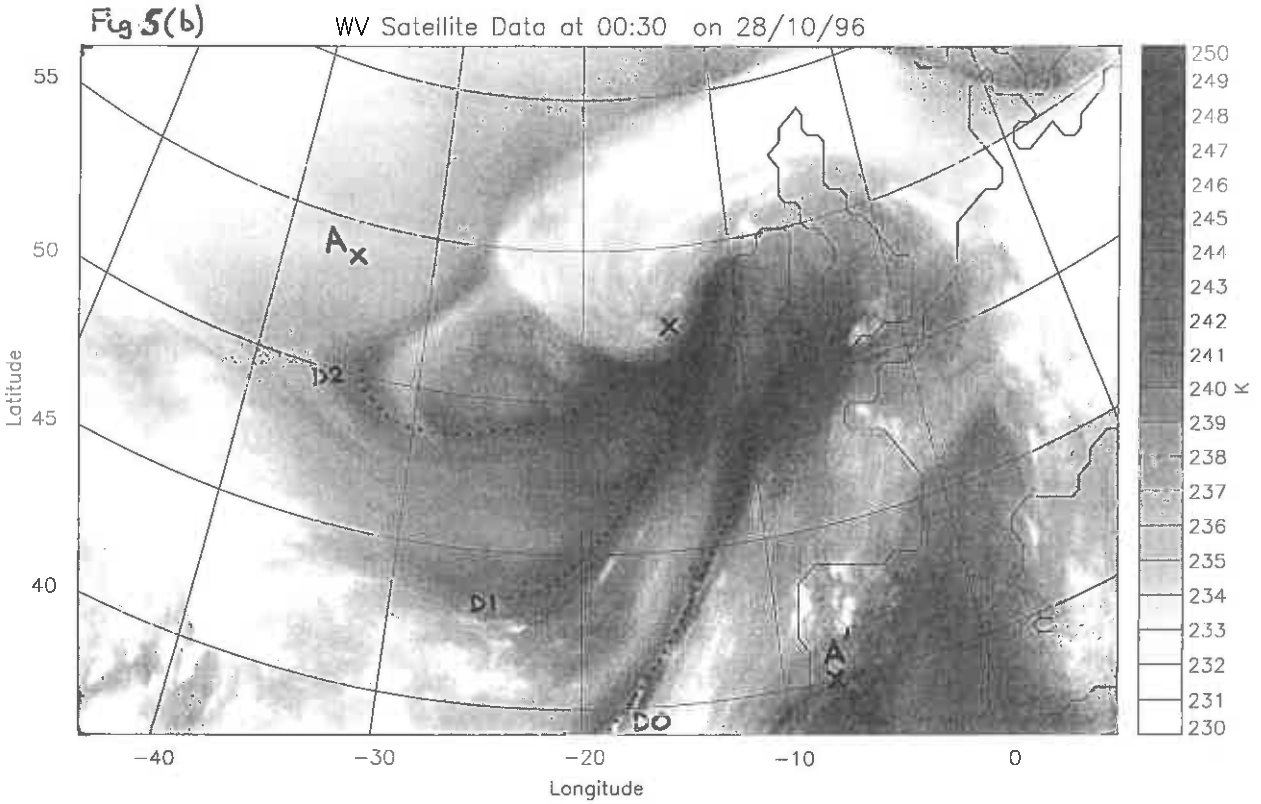
WV Satellite Data at 00:30 on 28/10/96
Latitude
55
50
45
40
A
X
D2
D1
D0
A
X
−40
−30
−20
−10
0
Longitude
250
249
248
247
246
245
244
243
242
241
240 K
239
238
237
236
235
234
233
232
231
230

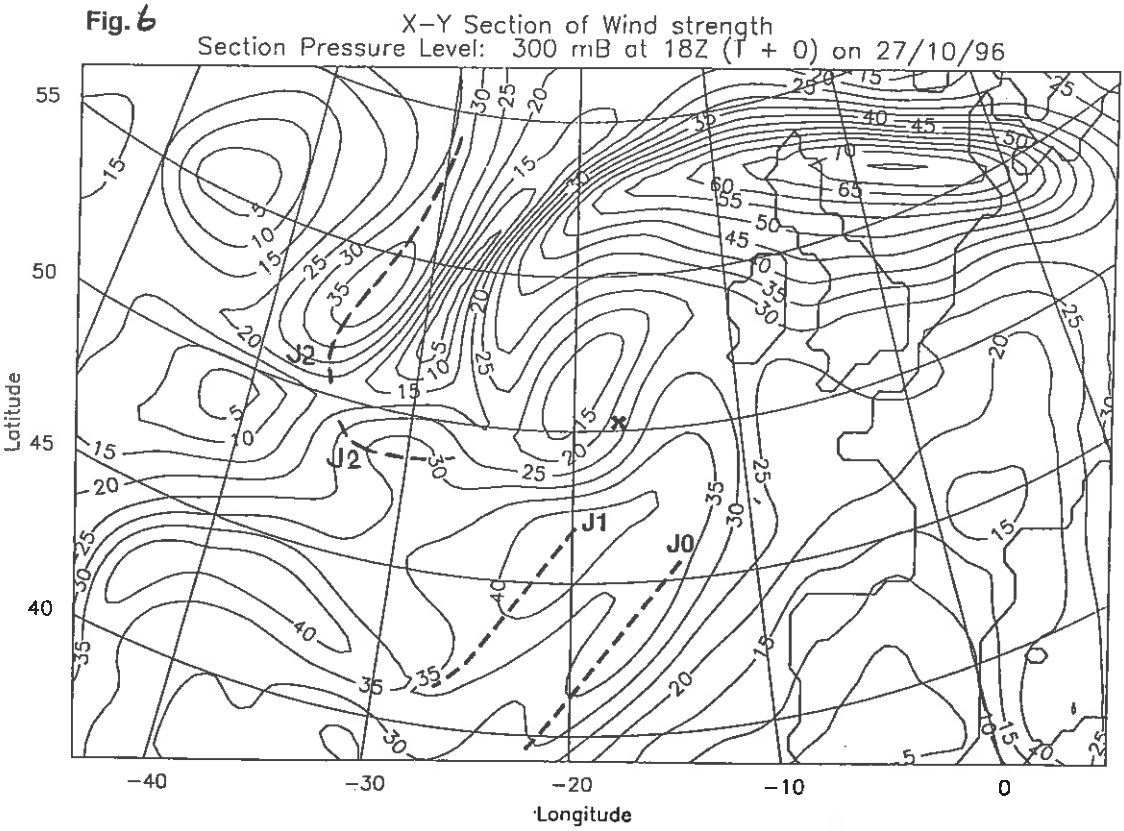

Fig. 6 Wind strength (in m s^{-1}) at 300 hPa, as derived from the UK Met Office Limited-Area model analysis for 18 UTC, 27 October 1996. The dashed lines draw attention to jet streaks JO, J1 and J2 (there are two parts to J2 as explained in the text). X marks the location of the cyclone centre.

Fig. 7

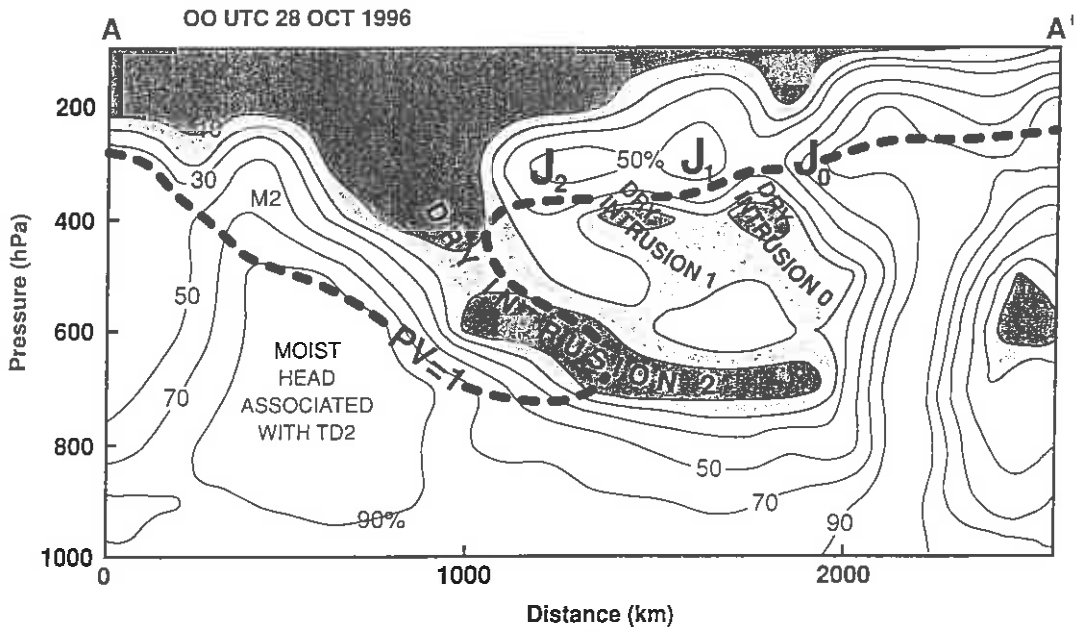

Fig.7 Vertical section along AA' in Figs.4(d) and 5(b) showing tracings of model results, as derived from the UK Met Office Limited-Area model analysis for 00 UTC, 28 October 1996, depicting relative humidity (with respect to ice where applicable), with isopleths at 10, 20, 30, 50, 70 and 90% (dark shading = dry) and potential vorticity, with isopleth of 1 PV unit shown as a thick dashed line. Also shown are axes of upper-level jets, labelled J1, J2 and J3; note that they are all associated with small wedges of moist air (as seen in the WV imagery).

Fig. 8

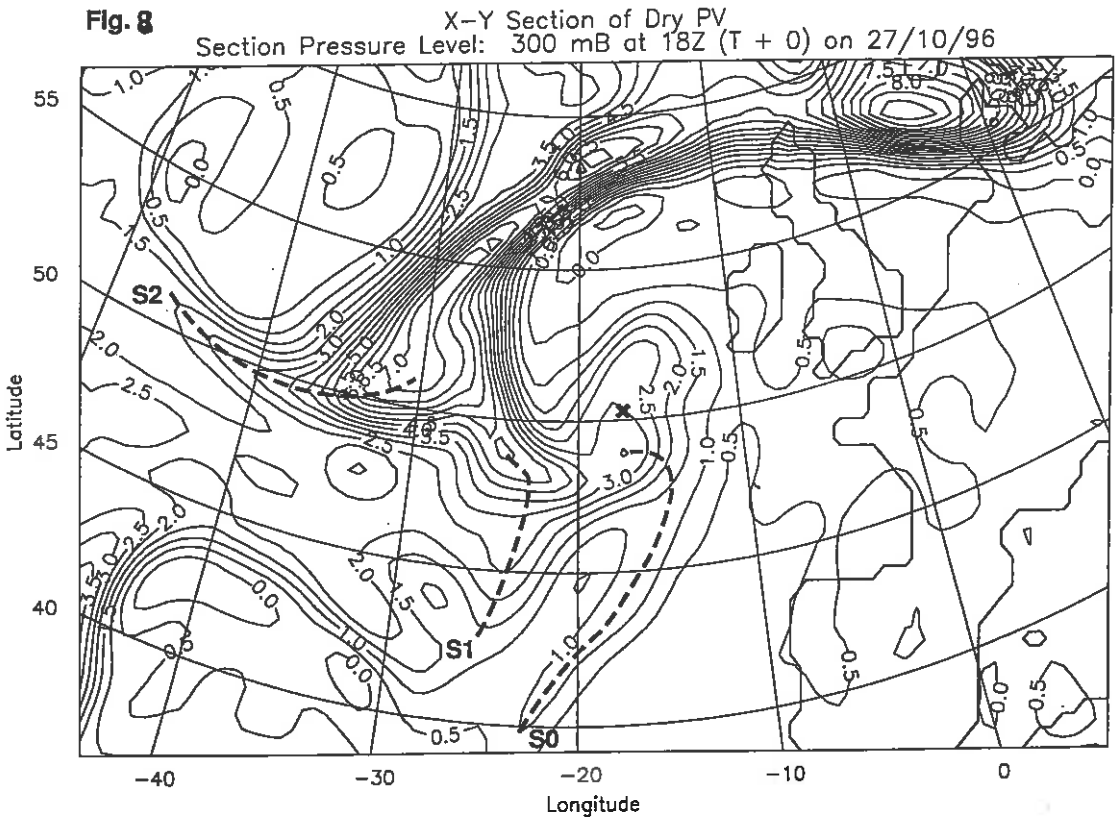

Fig.8 Potential vorticity (isopleths at intervals of 0.5 PV units) at 300 hPa, as derived from the UK Met Office Limited-Area model analysis for 18 UTC, 27 October 1996. The dashed lines draw attention to PV streamers S0, S1 and S2. These streamers are the upper-level manifestation of sheet-like PV maxima that extend downwards slantwise towards the south and east. Note the correspondence between the axes S0, S1, S2 and those of D0, D1 , D2, and J0, J1, J2 in Figs.5(a) (and 15) and 6, respectively.

Fig. 9

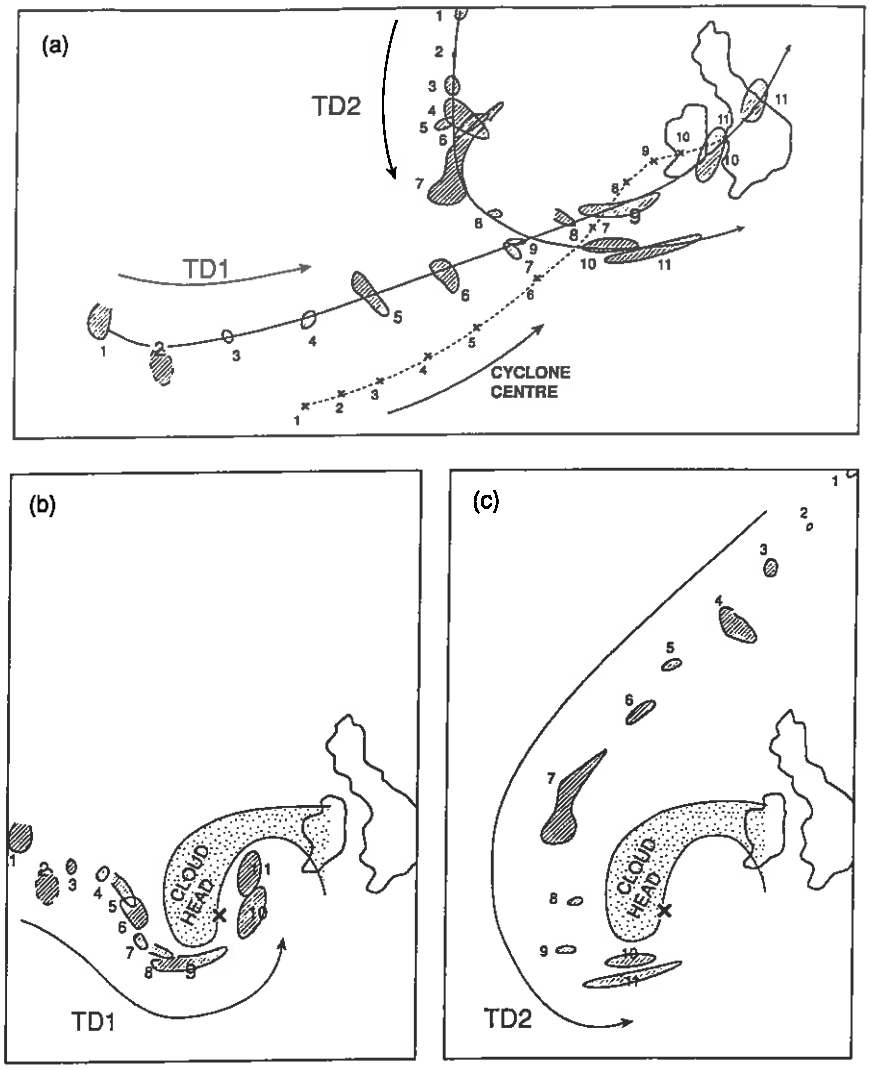

Fig.9 Tracks and intensity of mesoscale tropopause depressions TD1 and TD2 in relation to the cyclone centre as represented by their 300-hPa potential-vorticity cores at 6-hour intervals derived from UK Met Office Limited-Area model analyses between 06 UTC, 26 October and 18 UTC 28 October 1996. The time code used is in 6-hour steps with 1 corresponding to 26/06 and 11 corresponding to 28/18. (a): tracks of TD1 and TD2 relative to the Earth; also shown is the track of the cyclone centre (dotted line connecting crosses). (b and c): tracks of (b) TD1 and (c) TD2 relative to the cyclone centre. The positions of the cloud head (given here by mean the model's upper-level relative humidity > 75%), the British Isles coastline and the cyclone centre at 18 UTC, 27 October, are drawn in (b) and (c) for reference. The PV contours in (a), (b) and (c) are the highest integral-valued contours at each time. (d) and (e), respectively, show the 300 hPa PV of TD1 and TD2 and the mean sea level pressure of the cyclone over the period depicted in (a), (b) and (c). The bracketed value of mslp at 26/12 in (e) is at the time of a badly bogussed analysis and is thought to be grossly in error.

(d)

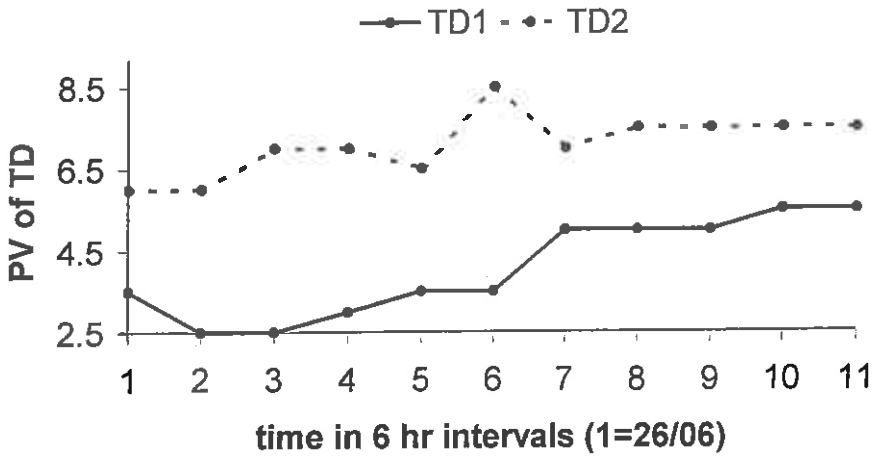
TD1
TD2
PV of TD
8.5
6.5
4.5
2.5
1 2 3 4 5 6 7 8 9 10 11
time in 6 hr intervals (1=26/06)

(e)

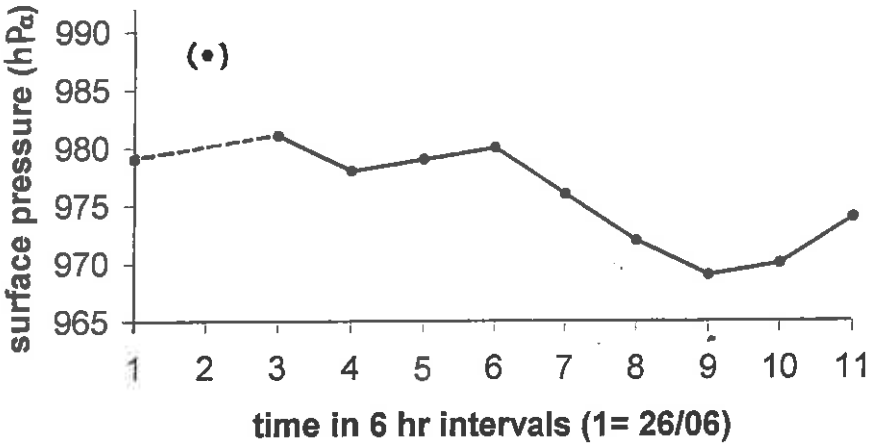
surface pressure (hPa)
990
985
980
975
970
965
1 2 3 4 5 6 7 8 9 10 11
time in 6 hr intervals (1= 26/06)

Figs 9 (d & e)

Fig 10

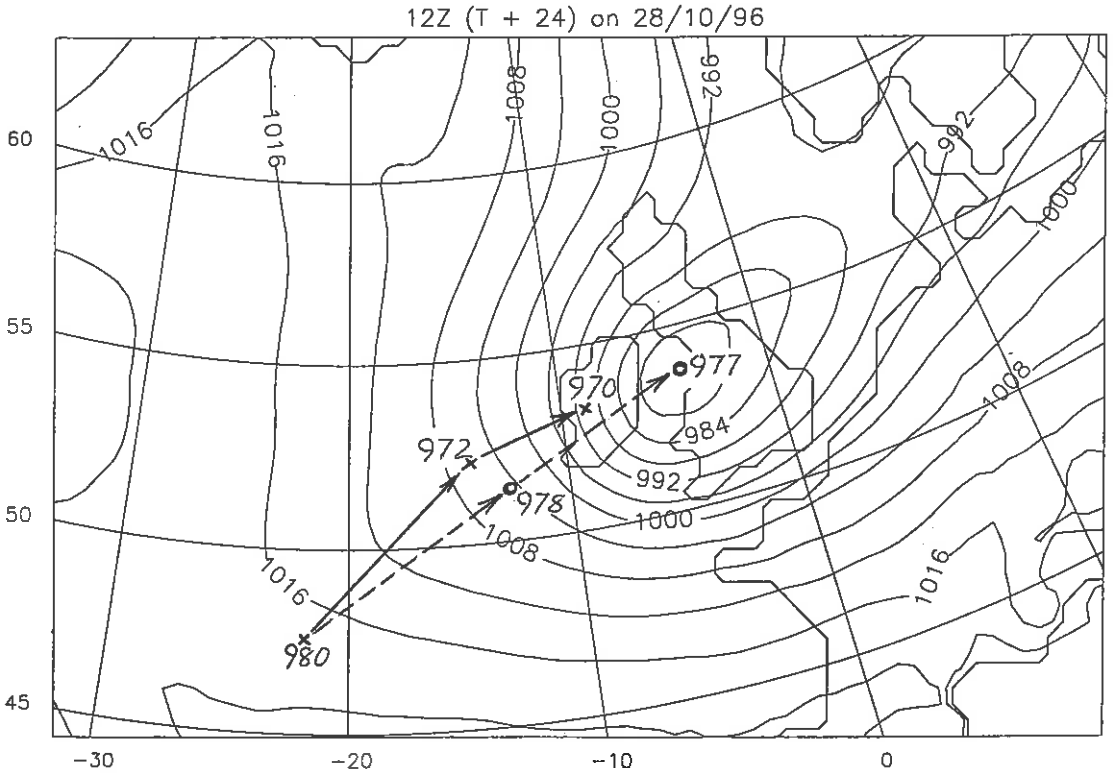

Fig.10 Comparison of analysed and forecast tracks of cyclone msl pressure centre superimposed on the 24-hour forecast pattern of msl pressure for 12 UTC, 28 October 1996, as derived from the operational run of the UK Met Office Limited-Area model. Solid lines and crosses with msl pressure labelled in hPa are from analyses at 12-hour intervals from 12 UTC, 27 October to 12 UTC, 28 October 1996. Dashed lines and circles, with msl pressure labelled, are from the forecast run made at 12 UTC, 27 October.

Fig. 11(a)

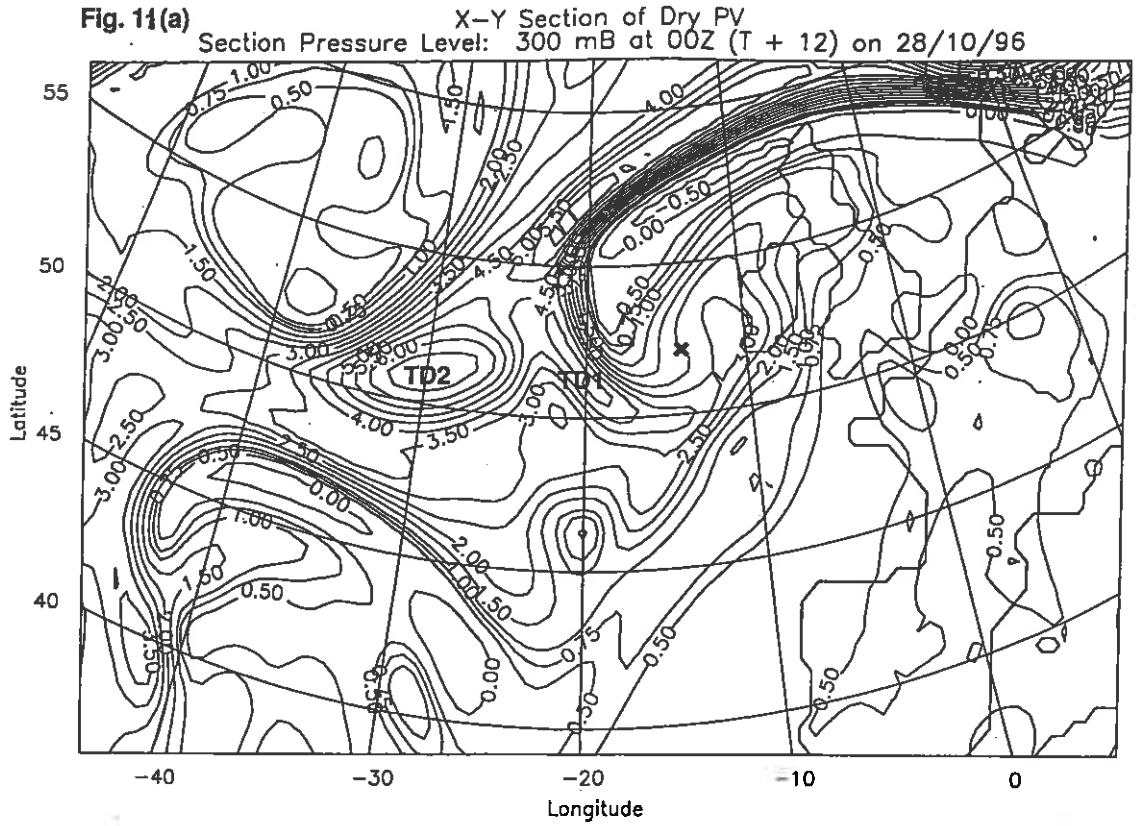

Fig. 11(b)

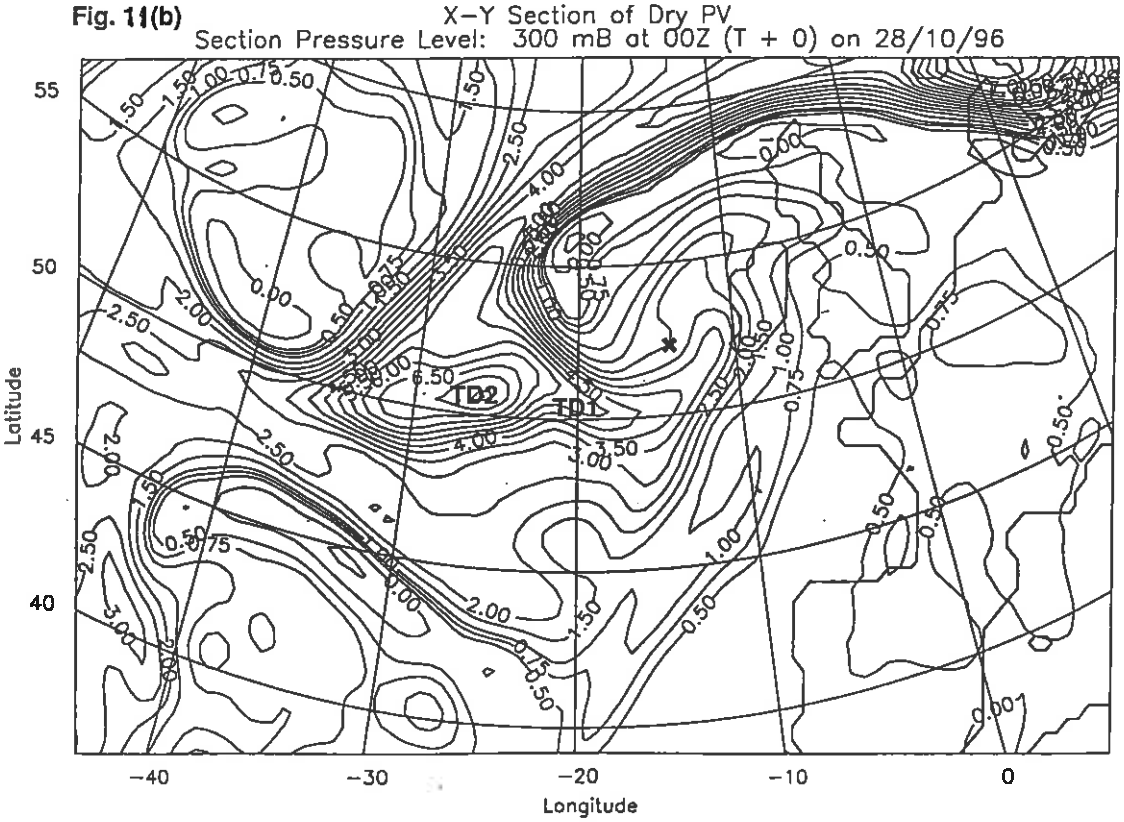

Fig.11 Comparison between the fields of potential vorticity at 300 hPa as obtained from (a) the operational 12-hour forecast verifying at 0 UTC, 28 October 1996 and (b) the analysis for 0 UTC 28 October, both from the UK Met Office Limited-Area Model. Both (a) and (b) show potential vorticity isopleths at intervals of 0.5 PV units plus one at 0.75: mesoscale tropopause depressions TD1 and TD2 are labelled. X shows the position of the cyclone msl pressure centre.

Fig. 12

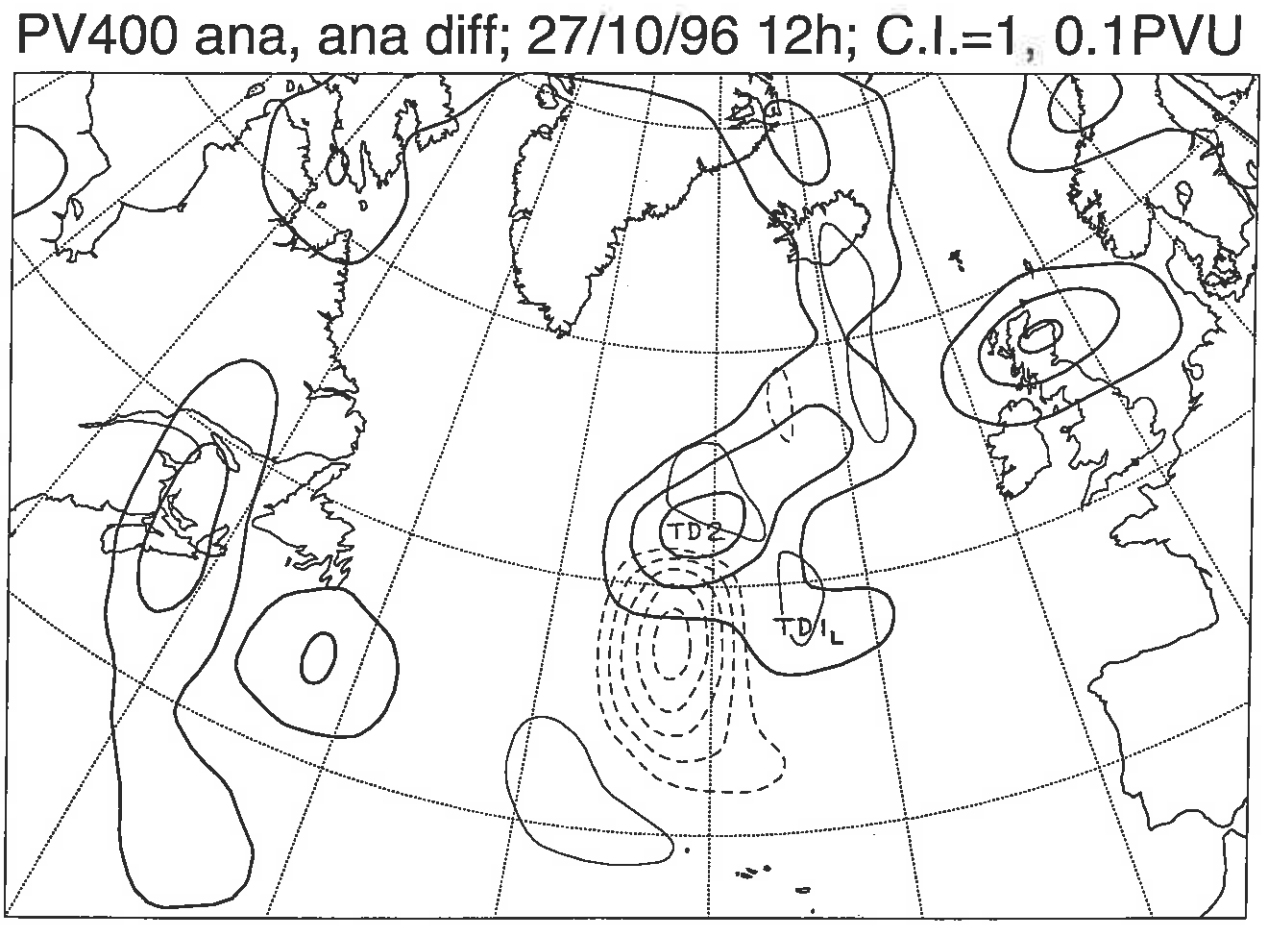

Fig. 12 Estimate of the ECMWF analysis error in potential vorticity valid at 12 UTC, 27 October 1996 (thin contours at intervals of 0.1 PV unit, the dashed contours indicating the need for a positive adjustment) superimposed on the unmodified operational ECMWF analysis of potential vorticity at 400 hPa (thick solid contours at intervals of 1 PV unit).

Fig 13

Fig 14

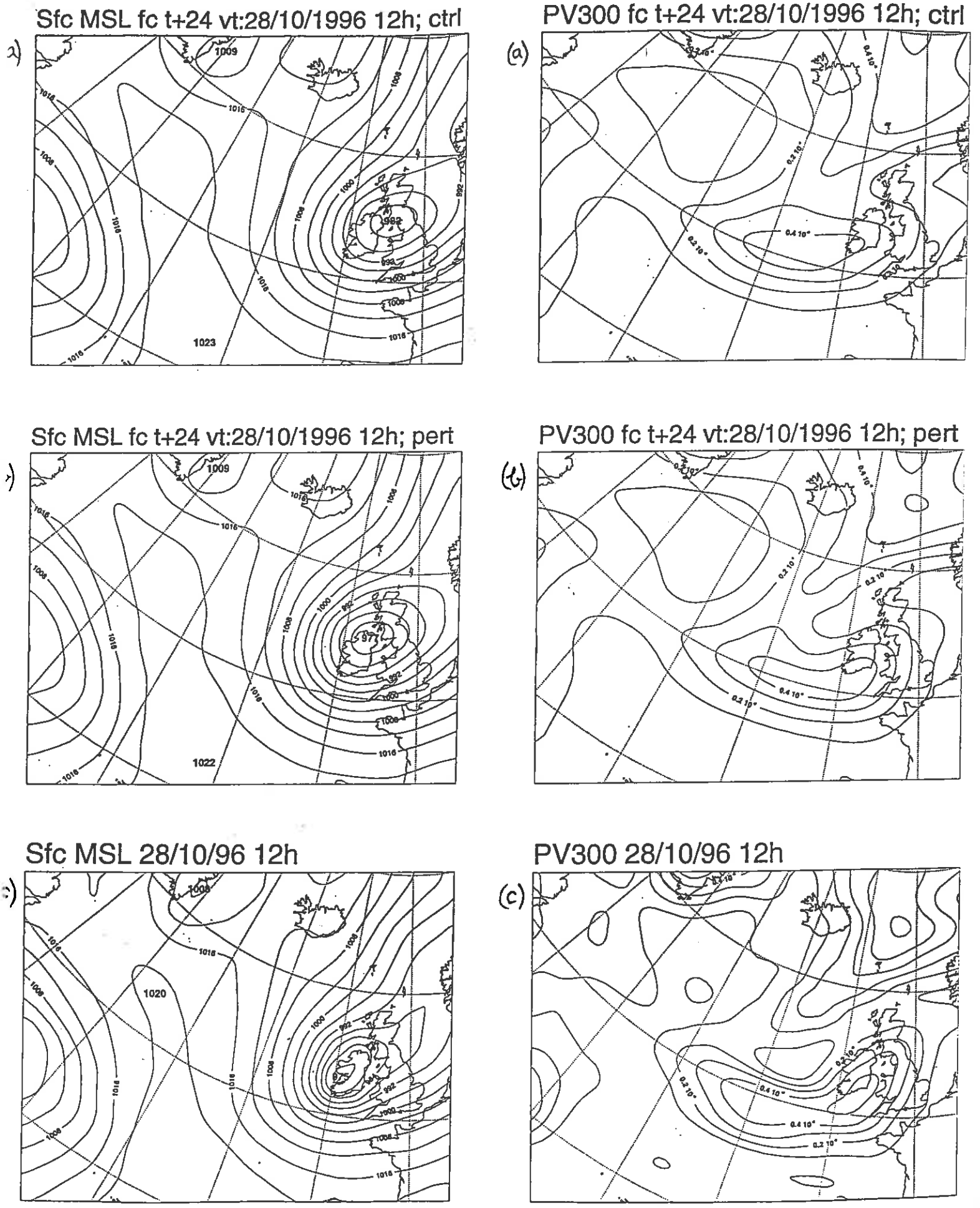

Fig.13 Comparison between the msl pressure patterns as obtained from (a) the operational 24-hour forecast verifying at 12 UTC, 28 October 1996, (b) the modified 24-hour forecast for the same time, and (c) the analysis for 12 UTC 28 October, all from the ECMWF model..

Fig.14 Similar comparisons as in Fig. 13 but for the fields of potential vorticity at 300 hPa. Potential vorticity contours are at intervals of 1 PV unit.

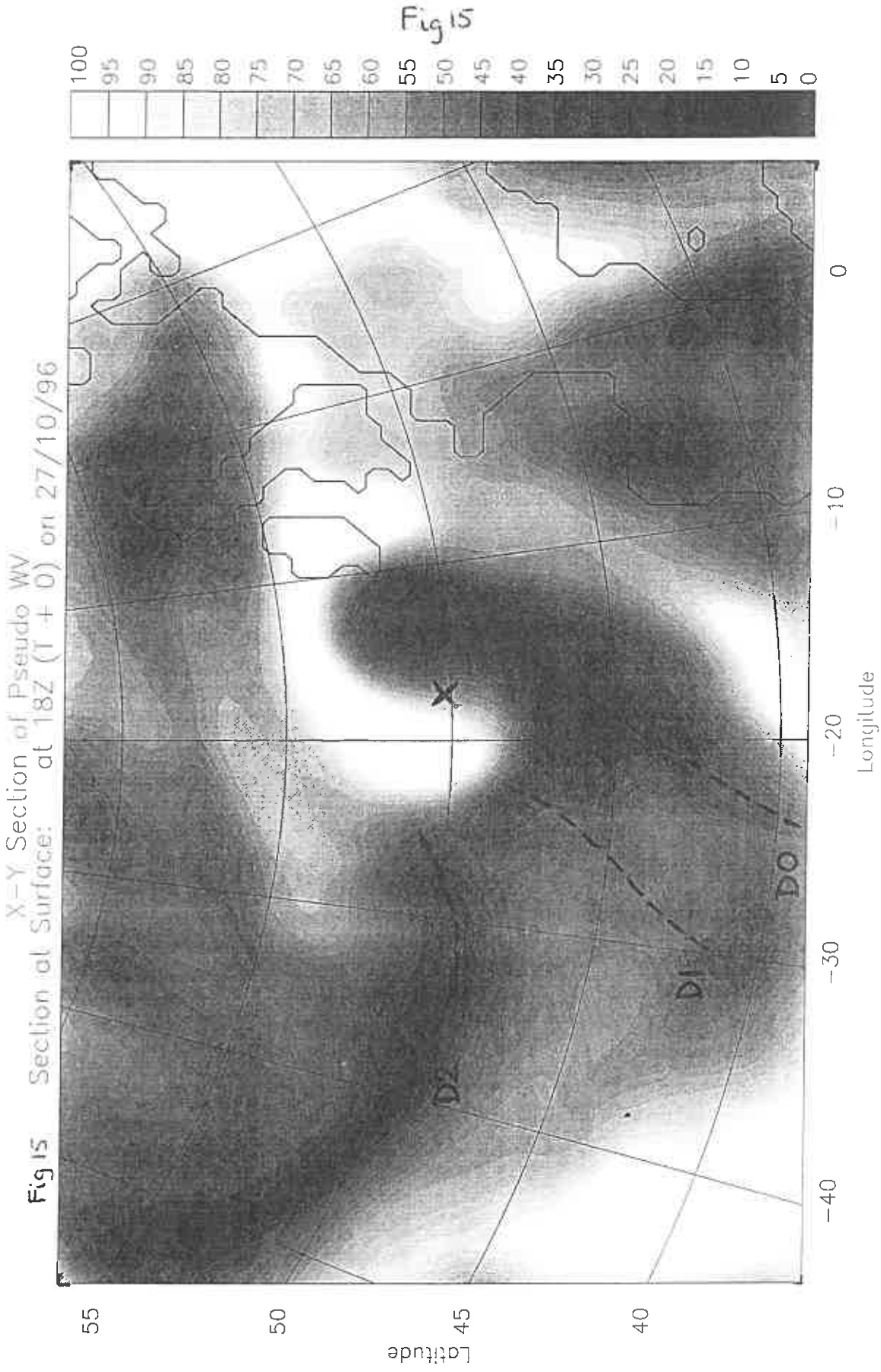

Fig. 15 Pseudo water vapor image derived as explained in the text from the UK Met Office Limited-Area model analysis for 18UTC, 27 October 1996. The dashed lines draw attention to the axes of the three dark zones corresponding to the upper parts of dry intrusions D0, D1 and D2. X marks the location of the cyclone centre.

Fig.16 Sequence of 6-hourly tracings from 12 UTC, 27 October until 12 UTC, 28 October 1996, showing salient features pertaining to the interaction between the cyclone and the second mesoscale tropopause depression (TD2), as derived from (a; left column) Meteosat water vapor imagery and (b; right column) UK Met Office Limited-Area Model analyses. To prevent overlap each tracing has been displaced by a constant offset from the previous one, as shown by the positions of the British Isles for the first two times. The north-south extent of the British Isles is about 900km. The hatched areas show the moist parts of the upper troposphere as given in (a) by brightness temperature below 237K in the water vapor channel and in (b) by an average relative humidity with respect to ice of 62.5% between 600 and 300 hPa. The main moist area is associated with the cyclone's main cloud head; the smaller moist area to the west (labelled M2), with hatching orientated at right angles to the rest, is associated with TD2. The bold lines in both (a) and (b) represent the axes of the 'dark zone' corresponding to the upper parts of dry intrusion 2 (labelled D2). The dotted contour in (b) represents the core of the upper-level vortex associated with TD2 as given by potential vorticity = 3 PV units at 400 hPa. The mesoscale tropopause depression TD2 became cut off at 300 hPa from the northern trough at 18 UTC, 27 October, after which V2 can be seen to maintain a well-defined spatial relationship to D2 and M2 on either side of it. The model-derived cyclone centre is denoted by X and the msl pressure is labelled in hPa, showing that the main period of deepening was between 12 UTC, 27 October and 06 UTC, 28 October.

Fig. 16

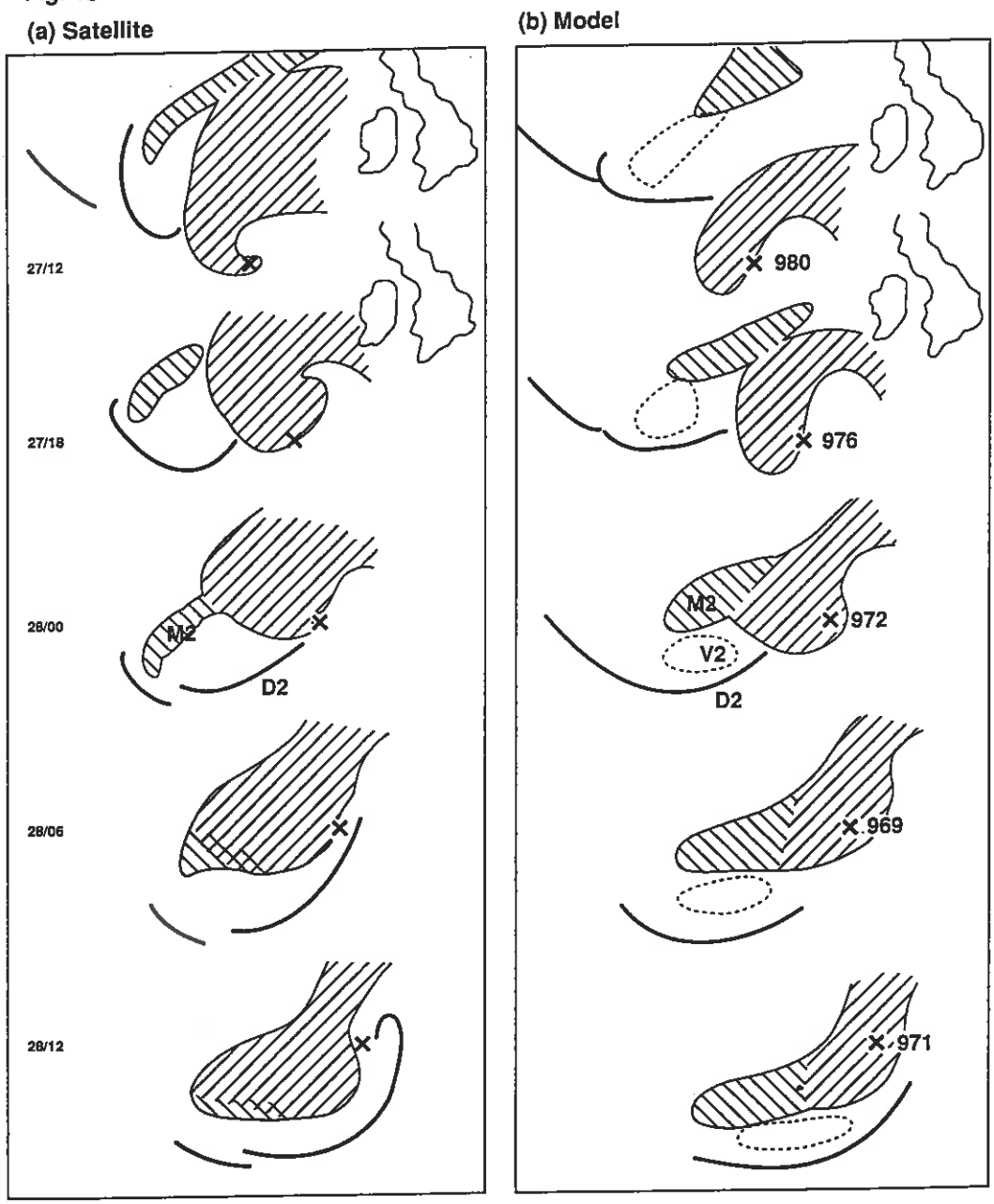
(a) Satellite
(b) Model
27/12
27/18
28/00
28/06
28/12
M2
D2
980
976
M2
V2
D2
972
969
971

Fig 17

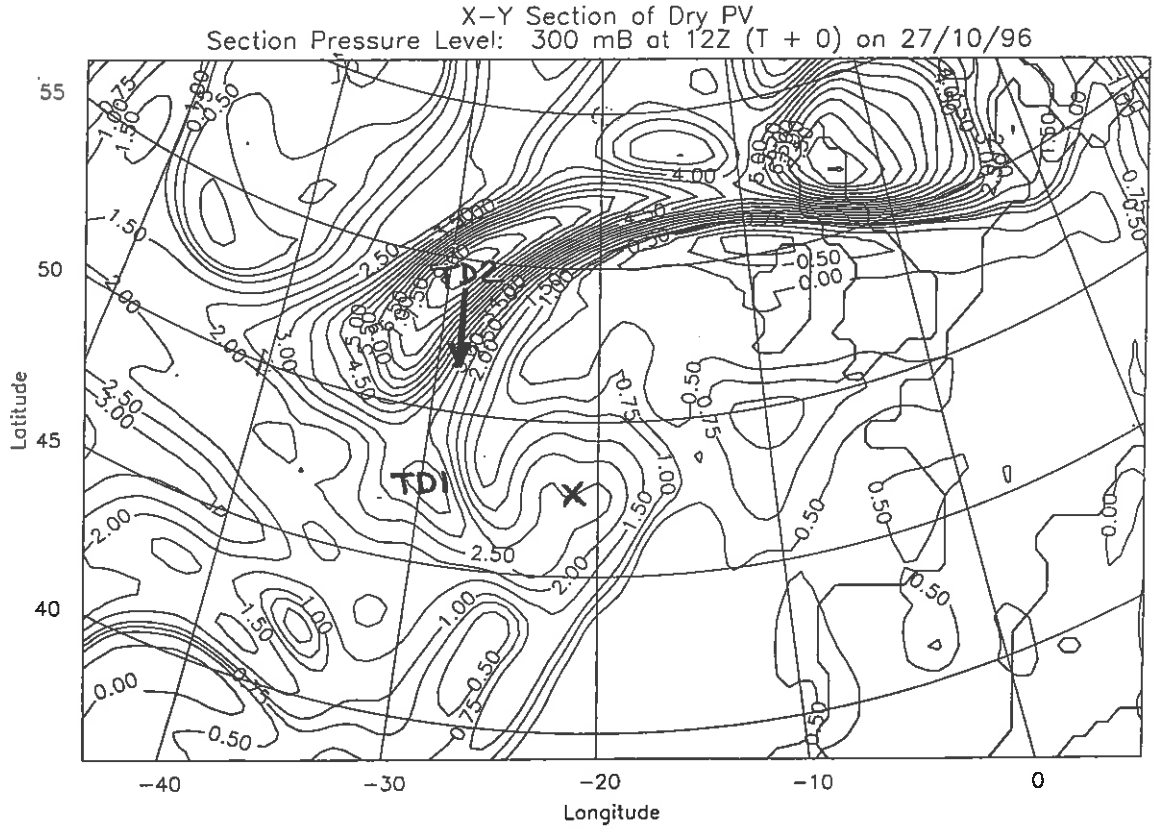

Fig.17 Field of potential vorticity at 300 hPa as obtained from the operational UK Met Office Limited-Area Model analysis at 12 UTC, 27 October 1996. Isopleths at intervals of 0.5 PV units plus one at 0.75 : mesoscale tropopause depressions TD1 and TD2 are labelled. The arrow denotes the 300 km displacement needing to be applied to TD2 to correct the error identified by comparison with WV imagery. X shows the analysed position of the cyclone msl pressure centre.

Fig. 18

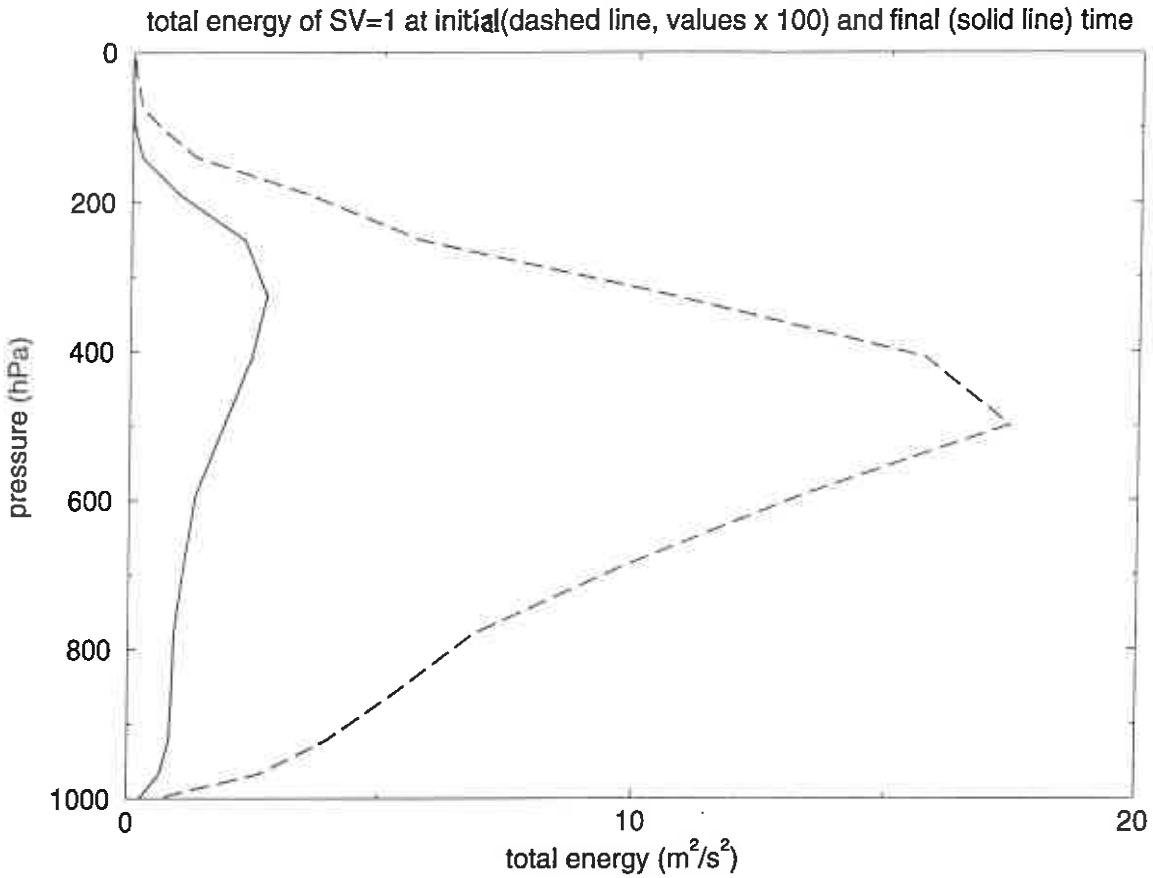

Fig 18 Vertical profile of total energy (in $m^2\ s^{-2}$) at the initial time, 12 UTC on 27 October 1996 (dashed line, values multiplied by 100) and at the final time, 12 UTC on 28 October (solid line) for the first 24-hour singular vector, based upon the ECMWF model.

Fig 19

961027oc27 T0 PV -SV= 1-L= 9-F=0.100E+10-D=0.600E+01

(a)

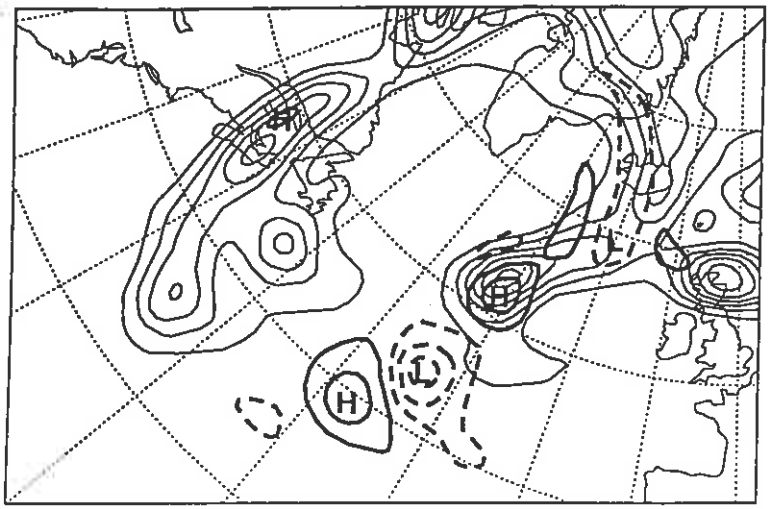

961027oc27 T0 PV -SV= 1-L=10-F=0.100E+10-D=0.600E+01

(b)

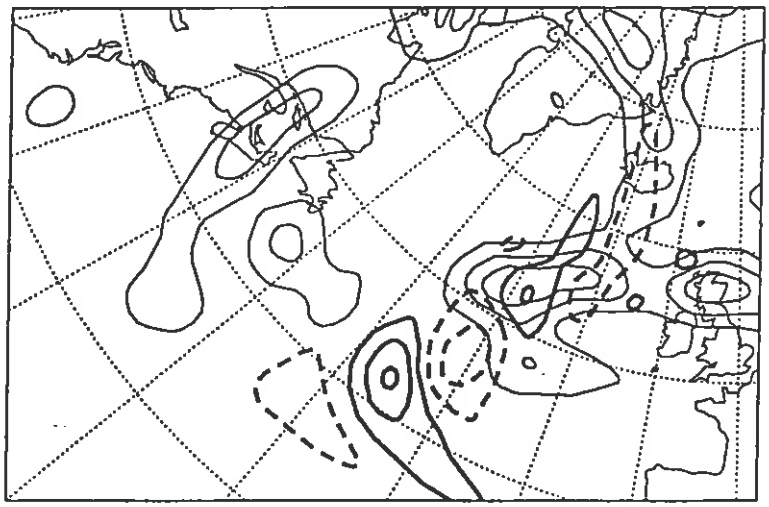

Fig.19 Sensitive regions (in PV) inferred from the first singular vector in the ECMWF model, superimposed on the basic-state analysis of PV, for 12 UTC, 27 October 1996 at (a) 325, and (b) 400 hPa. Thick contours indicate SV structure (solid, positive; dashed, negative) with contour interval 0.006 PV units. Thin contours indicate basic-state PV, with a contour interval of 1 PV unit.

Fig 20

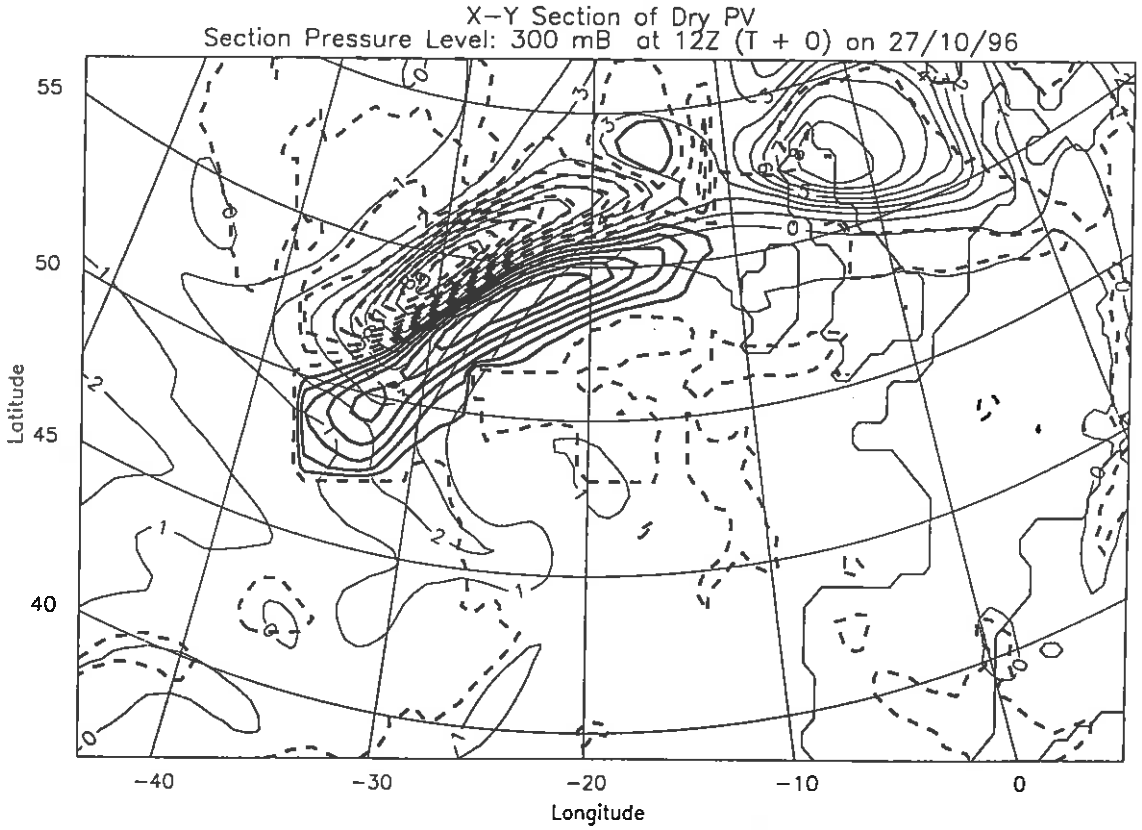

Fig.20 Estimate of the UK Met Office analysis error in potential vorticity valid at 12 UTC, 27 October 1996 (thick contours at intervals of 1 PV unit; solid positive, dashed negative) superimposed on the unmodified operational UK Met Office Limited-Area Model analysis of potential vorticity at 300 hPa (thin solid contour at intervals of 1PV unit). The operational analysis shown here differs slightly from that shown in Fig. 17 for reasonsthat are explained in the text.

Fig 21

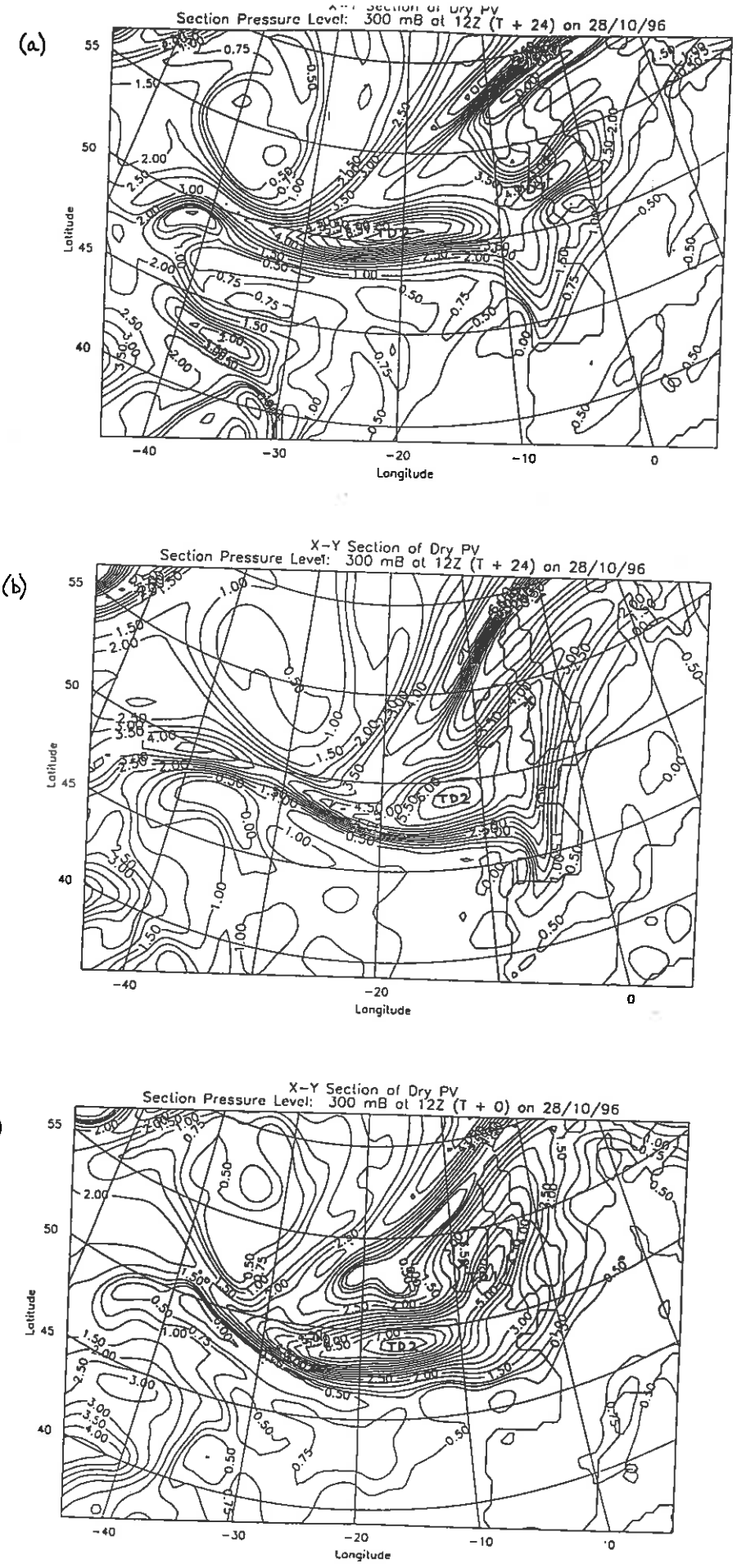

Fig.21 Comparison between the fields of potential vorticity at 300 hPa as obtained from (a) the operational 24-hour forecast (FOP) verifying at 0 UTC, 28 October 1996, (b) the modified 24-hour forecast (FMOD) for the same time and (c) the analysis for 0 UTC 28 October, all from the UK Met Office Limited-Area Model. Same format as in Fig.11 See text in Section 6 for explanation of the modification underlying (b).

CURRENT JCMM INTERNAL REPORTS

This series of JCMM Internal Reports, initiated in 1993, contains unpublished reports and also versions of articles submitted for publication. The complete set of Internal Reports is available from the National Meteorological Library on loan, if required.

1. **Research strategy and programme**
   K A Browning et al
   January 1993

2. **The GEWEX Cloud System Study (GCSS)**
   GEWEX Cloud System Science Team
   January 1993

3. **Evolution of a mesoscale upper tropospheric vorticity maximum and comma cloud from a cloud-free two dimensional potential vorticity anomaly**
   K A Browning
   January 1993

4. **The global energy and water cycle**
   K A Browning
   July 1993

5. **Structure of a midlatitude cyclone before occlusion**
   K A Browning and N Roberts
   July 1993

6. **Developments in systems and tools for weather forecasting**
   K A Browning and G Szejwach
   July 1993

7. **Diagnostic study of a narrow cold frontal rainband and severe winds associated with a stratospheric intrusion**
   K A Browning and R Reynolds
   August 1993

8. **Survey of perceived priority issues in the parametrizations of cloud-related processes in GCMs**
   K A Browning
   September 1993

9. **The effect of rain on longwave radiation**
   I Dharssi
   September 1993

10. **Cloud microphysical processes - a description of the parametrization used in the large eddy model**
    H Swann
    October 1993

11. **An appreciation of the meteorological research of Ernst Kleinschmidt**
    A J Thorpe
    May 1992

12. **Potential vorticity of flow along the Alps**
    A J Thorpe, H Volkert and Dietrich Heimann
    August 1992

13. **The representation of fronts**
    A J Thorpe
    January 1993

14. **A parametrization scheme for symmetric instability: test for an idealised flow**
C S Chan and A J Thorpe
February 1993

15. **The Fronts 92 Experiment: a Quicklook Atlas**
Edited by T D Hewson
November 1993

16. **Frontal wave stability during moist deformation frontogenesis**
Part 1: Linear wave dynamics
C H Bishop and A J Thorpe
May 1993

17. **Frontal wave stability during moist deformation frontogenesis**
Part 2. The suppression of non-linear wave development
C H Bishop and A J Thorpe
May 1993

18. **Gravity waves in sheared ducts**
S Monserrat and A J Thorpe
October 1993

19. **Potential vorticity and the electrostatics analogy: quasi-geostrophic theory**
C Bishop and A J Thorpe
November 1993

20. **Recent advances in the measurement of precipitation by radar**
A J Illingworth
April 1993

21. **Micro-physique et givrage: cloud microphysics and aircraft icing**
A J Illingworth
May 1993

22. **Differential phase measurements of precipitation**
M Blackman and A J Illingworth
May 1993

23. **Estimation of effective radius of cloud particles from the radar reflectivity**
N I Fox and A J Illingworth
May 1993

24. **A simple method of Dopplerising a pulsed magnetron radar**
A Hua, A J Illingworth and J Eastment
November 1993

25. **Radiation and polar lows**
George C Craig
February 1994

26. **Collected preprints submitted to the International Symposium on the Life Cycles of Extratropical Cyclones; Bergen, Norway, 27 June - 1 July 1994**
April 1994

27. **Convective frontogenesis**
Douglas J Parker and Alan J Thorpe
April 1994

28. **Improved measurement of the ice water content in cirrus using a total water evaporator**
Philip R A Brown and Peter N Francis
April 1994

29. **Mesoscale effects of a dry intrusion within a vigorous cyclone**
K A Browning and B W Golding
April 1994

30. **GEWEX Cloud System Study, Science Plan**
May 1994

31. **Parametrization of momentum transport by convectively generated gravity waves**
R Kershaw
May 1994

32. **Mesoscale Modelling Newsletter No 5**
May 1994

33. **Observations of the mesoscale sub-structure in the cold air of a developing frontal cyclone**
K A Browning, S A Clough, C S A Davitt, N M Roberts and T D Hewson
May 1994

34. **Longwave radiative forcing of a simulated tropical squall line**
Imtiaz Dharssi
July 1994

35. **On the nature of the convective circulation at a kata-cold front**
K A Browning
September 1994

36. **Collective preprints of papers submitted to the COST-75 International Seminar on Advanced Weather Radar Systems, Brussels, 20-23 September 1994**
November 1994

37. **Use of satellite imagery to diagnose events leading to frontal thunderstorms: Parts I and II of a case study**
K A Browning and N M Roberts
November 1994

38. **The role of spaceborne millimetre-wave radar in the global monitoring of ice cloud**
P R A Brown, A J Illingworth, A J Heymsfield, G M McFarquhar, K A Browning and M Gosset
December 1994

39. **Potential vorticity inversion**
Michal Ziemianski
October 1994

40. **Theory of mature tropical cyclones; a comparison between Kleinschmidt (1951) and Emanuel (1986)**
Suzanne L Gray
December 1994

41. **Dispersion and removal of pollutants during the passage of an atmospheric frontal system**
N R Gimson
December 1994

42. **The role of snow sublimation in frontogenesis**
D J Parker and A J Thorpe
December 1994

43. **Potential vorticity and the electrostatics Analogy: Ertel-Rossby formulation**
A J Thorpe and C H Bishop
December 1994

44. **Mesoscale aspect of extratropical cyclones: an observational perspective**
K A Browning
January 1995

45. **A polar low outbreak: evolution and mesoscale structures**
T D Hewson, G C Craig and C Claud
February 1995

46. **Generation of near-surface gusts of deep convection**
K Nakamura and R Kershaw
April 1995

47. **Attribution concepts applied to the Omega Equation**
S A Clough, C S A Davitt and A J Thorpe
June 1995

48. **Parametrization of mixed-phase cloud and precipitation**
Susan P Ballard and M Gerard Hutchinson
June 1995

49. **Short-range forecasting of stratocumulus: initialization prediction**
Susan P Ballard, Simon D Jackson and B Macpherson
June 1995

50. **Contributions of the JCMM/Dept of Meteorology Radar Group to the 27th AMS Radar Meteorology Conference, Vail October 1995**
June 1995

51. **Cold pools in shear**
Douglas J Parker
September 1995

52. **High-resolution analysis of frontal fracture**
K A Browning, S P Ballard and C S A Davitt
September 1995

53. **The albedo of broken cloud fields: calculations using a modified two stream radiation code**
Imtiaz Dharssi and Roy Kershaw
October 1995

54. **Parametrization of momentum transport by convection. I: theory and cloud modelling results**
R Kershaw and D Gregory
November 1995

55. **Variation of frontal structure along a cold front**
K A Browning and N M Roberts
November 1995

56. **Secondary frontal waves**
Douglas Parker
December 1995

57. **Objective fronts**
T D Hewson
March 1996

58. **Mesoscale analysis of the activation of a cold front during cyclogenesis**
K A Browning, N M Roberts and A J Illingworth
June 1996

59. **Investigation of different representations of rain in a 1-d evaporation model**
H Swann
May 1996

60. **Parametrization of diabatic processes in the inversion of the omega-equation**
M Athanassiadou and A J Thorpe
June 1996

61. **The role of the environmental flow in the development of secondary frontal cyclones**
I A Renfrew, A J Thorpe and A Joly
June 1996

62. **Consequences of the geostrophic momentum approximation on barotropic instability**
S Malardel, A J Thorpe and A Joly
June 1996

63. **Contributions to the AMS/RMS Conference on Mesoscale Processes**
Reading, 9-13 September 1996

64. **Vorticity and potential vorticity in stratified flows interacting with an isolated obstacle**
Jorge A Gutiérrez and A J Thorpe
September 1996

65. **Triple point development: two case studies**
Douglas Parker
September 1996

66. **Radar observations of wind-shear splitting within evolving atmospheric Kelvin-Helmholtz billows**
D Chapman and K A Browning
April 1997

67. **Cold frontal structure derived from radar wind profilers**
K A Browning, D Jerrett, J Nash, T Oakley and N M Roberts
May 1997

68. **The dry intrusion and its effect on the frontal, cloud and precipitation structure of extratropical cyclones**
K A Browning - Text of invited special lecture at the Spring Conference
of the Meteorological Society of Japan, University of Tsukuba, 22 May 1997

69. **Met. Office Unified Model data, diagnostics, graphics programs, and other observational data available from the JCMM through the aegis of the Universities Weather Research Network (UWERN).** (Plus supplement)
Peter Panagi and Ed Dicks
June 1997

70. **Contributions of the JCMM/Dept of Meteorology Radar Group to the 28th AMS Radar Meteorology Conference.** Austin, Texas
September 1997

71. **Sensitivity of short-range weather forecasts to local potential vorticity modifications**
Meral Demirtas and Alan Thorpe
July 1997

72. **Objective identification of frontal wave cyclones**
T D Hewson
August 1997

73. **Attribution and its application to mesoscale structure associated with tropopause folds**
A J Thorpe
September 1997

74. **The role of the environmental flow in the development of secondary frontal cyclones**
Ian A Renfrew, Alan J Thorpe and Craig H Bishop
September 1997

75. **Potential vorticity: a short history of its definitions and uses**
Alan J Thorpe and Hans Volkert
September 1997

76. **Superposing semi-geostrophic potential vorticity anomalies**
H R Birkett and A J Thorpe
September 1997

77. **Short period forecasting of catchment-scale precipitation.**
Part 1: the role of Numerical Weather Prediction
M A Pedder, M Haile and A J Thorpe
September 1997

78. **Verification of the tracking technique used in an experimental cloud motion wind inferring system**
Z Wang, K A Browning and G A Kelly
October 1997

79. **A preliminary study of Fourier series analysis for cloud tracking with GOES high temporal resolution images**
Z Wang
October 1997

80. **Analysis of an ex-tropical cyclone after reintensifying as a warm-core extratropical cyclone**
K A Browning, G Vaughan and P Panagi
November 1997

81. **A JCMM overview of FASTEX IOPs**
S A Clough, H W Lean, N M Roberts, H Birkett, J-P Chaboureau, R Dixon, M Griffiths, T D Hewson and A Montani
January 1998

82. **Programs for PV inversion and modification**
Meral Demirtas
December 1997

83. **Release of potential shearing instability in warm frontal zones**
D Chapman and K A Browning
February 1998

84. **The European Cloud-Resolving Modelling Programme (EUCREM)**
Summary Report from the coordinator
P W White
April 1998

85. **A frontal wave database**
T D Hewson
April 1998

86. **Layering observed in dropsoundings from IOP 1 of Fronts 92**
S A Clough
May 1998

87. **Use of wind-shear displays for Doppler radar data**
D Chapman and K A Browning
May 1998

88. **Radar estimates of rainfall rates at the ground in bright band and non-bright band events**
T J Smyth and A J Illingworth
June 1998

89. **Correction for attenuation of radar reflectivity using polarisation data**
T J Smyth and A J Illingworth
June 1998

90. **The effects of convection on chemical reactions and precipitation scavenging**
Neil R Gimson
July 1998

91. **How to use the display program DISP**
Nigel Roberts
August 1998

92. **Conceptual models of cyclogenesis**
Adrian T Semple
August 1998

93. **Observations of oblate hail using dual polarisation radar and implications for hail detection schemes**
T J Smyth, T M Blackman and A J Illingworth
September 1998

94. **The semigeostrophic diagnosis of vertical motion. Part I: Formulation and co-ordinate transformations**
Mike A Pedder and Alan J Thorpe
September 1998

95. **The semigeostrophic diagnosis of vertical motion. Part II: Results for an idealised baroclinic wave life cycle**
Alan J Thorpe and Mike A Pedder
September 1998

96. **Convective destabilisation by a tropopause fold diagnosed using potential vorticity inversion**
Morwenna Griffiths, Alan Thorpe and Keith Browning
October 1998

97. **Forecast skill of the ECMWF model using targeted observations during FASTEX**
A Montani, A J Thorpe, R Buizza and P Unden
October 1998

98. **Observations and model simulations of the FASTEX IOP 16 frontal wave - effects of sublimation**
Sid A Clough, Humphrey W Lean, Nigel M Roberts and Richard M Forbes
December 1998

99. **The application of conceptual models in NWP**
Adrian T Semple
January 1999

100. **Mesoscale analysis of arc rainbands in a dry slot**
K A Browning and N M Roberts
January 1999

101. **Interaction of mesoscale tropopause depressions with a warm-core cyclone: observational and model analyses, and sensitivity to analysis errors**
K A Browning, A J Thorpe, A Montani, D Parsons, M Griffiths, P Panagi and E M Dicks
February 1999

Met Office Joint Centre for Mesoscale Meteorology Department of Meteorology
University of Reading PO Box 243 Reading RG6 6BB United Kingdom
Tel: +44 (0)118 931 8425 Fax: +44 (0)118 931 8791
www.metoffice.com